DESY 94-143

Measurement of the proton structure function F_2 from the 1993 HERA data

ZEUS Collaboration

Revised Sept. 23 1994

Abstract

The ZEUS detector has been used to measure the proton structure function F_2. During 1993 HERA collided 26.7 GeV electrons on 820 GeV protons. The data sample corresponds to an integrated luminosity of 0.54 pb^{-1}, representing a twenty fold increase in statistics compared to that of 1992. Results are presented for $7 < Q^2 < 10^4$ GeV^2 and x values as low as 3×10^{-4}. The rapid rise in F_2 as x decreases observed previously is now studied in greater detail and persists for Q^2 values up to 500 GeV^2.

The ZEUS Collaboration

M. Derrick, D. Krakauer, S. Magill, B. Musgrave, J. Repond, J. Schlereth, R. Stanek, R.L. Talaga, J. Thron
Argonne National Laboratory, Argonne, IL, USA [p]

F. Arzarello, R. Ayad[1], G. Bari, M. Basile, L. Bellagamba, D. Boscherini, A. Bruni, G. Bruni, P. Bruni, G. Cara Romeo, G. Castellini[2], M. Chiarini, L. Cifarelli[3], F. Cindolo, F. Ciralli, A. Contin, S. D'Auria, F. Frasconi, P. Giusti, G. Iacobucci, G. Laurenti, G. Levi, A. Margotti, T. Massam, R. Nania, C. Nemoz, F. Palmonari, A. Polini, G. Sartorelli, R. Timellini, Y. Zamora Garcia[1], A. Zichichi
University and INFN Bologna, Bologna, Italy [f]

A. Bargende, J. Crittenden, K. Desch, B. Diekmann, T. Doeker, L. Feld, A. Frey, M. Geerts, G. Geitz, M. Grothe, H. Hartmann, D. Haun, K. Heinloth, E. Hilger, H.-P. Jakob, U.F. Katz, S.M. Mari, A. Mass, S. Mengel, J. Mollen, E. Paul, Ch. Rembser, R. Schattevoy[4], J.-L. Schneider[4], D. Schramm, J. Stamm, R. Wedemeyer
Physikalisches Institut der Universität Bonn, Bonn, Federal Republic of Germany [c]

S. Campbell-Robson, A. Cassidy, N. Dyce, B. Foster, S. George, R. Gilmore, G.P. Heath, H.F. Heath, T.J. Llewellyn, C.J.S. Morgado, D.J.P. Norman, J.A. O'Mara, R.J. Tapper, S.S. Wilson, R. Yoshida
H.H. Wills Physics Laboratory, University of Bristol, Bristol, U.K. [o]

R.R. Rau
Brookhaven National Laboratory, Upton, L.I., USA [p]

M. Arneodo, L. Iannotti, M. Schioppa, G. Susinno
Calabria University, Physics Dept.and INFN, Cosenza, Italy [f]

A. Bernstein, A. Caldwell, I. Gialas, J.A. Parsons, S. Ritz, F. Sciulli, P.B. Straub, L. Wai, S. Yang
Columbia University, Nevis Labs., Irvington on Hudson, N.Y., USA [q]

P. Borzemski, J. Chwastowski, A. Eskreys, K. Piotrzkowski, M. Zachara, L. Zawiejski
Inst. of Nuclear Physics, Cracow, Poland [j]

L. Adamczyk, B. Bednarek, K. Eskreys, K. Jeleń, D. Kisielewska, T. Kowalski, E. Rulikowska-Zarębska, L. Suszycki, J. Zając
Faculty of Physics and Nuclear Techniques, Academy of Mining and Metallurgy, Cracow, Poland [j]

T. Kędzierski, A. Kotański, M. Przybycień
Jagellonian Univ., Dept. of Physics, Cracow, Poland [k]

L.A.T. Bauerdick, U. Behrens, J.K. Bienlein, S. Böttcher, C. Coldewey, G. Drews, M. Flasiński[5], D.J. Gilkinson, P. Göttlicher, B. Gutjahr, T. Haas, L. Hagge, W. Hain, D. Hasell, H. Heßling, H. Hultschig, Y. Iga, P. Joos, M. Kasemann, R. Klanner, W. Koch, L. Köpke, U. Kötz, H. Kowalski, W. Kröger[6], J. Krüger[4], J. Labs, A. Ladage, B. Löhr, M. Löwe, D. Lüke, J. Mainusch, O. Mańczak, J.S.T. Ng, S. Nickel, D. Notz, K. Ohrenberg, M. Roco, M. Rohde, J. Roldán[7], U. Schneekloth, W. Schulz, F. Selonke, E. Stiliaris[7], T. Voß, D. Westphal, G. Wolf, C. Youngman
Deutsches Elektronen-Synchrotron DESY, Hamburg, Federal Republic of Germany

H.J. Grabosch, A. Leich, A. Meyer, C. Rethfeldt, S. Schlenstedt
DESY-Zeuthen, Inst. für Hochenergiephysik, Zeuthen, Federal Republic of Germany

G. Barbagli, P. Pelfer
University and INFN, Florence, Italy [f]

G. Anzivino, G. Maccarrone, S. De Pasquale, S. Qian, L. Votano
INFN, Laboratori Nazionali di Frascati, Frascati, Italy [f]

A. Bamberger, A. Freidhof, T. Poser[8], S. Söldner-Rembold, J. Schroeder, G. Theisen, T. Trefzger
Fakultät für Physik der Universität Freiburg i.Br., Freiburg i.Br., Federal Republic of Germany [c]

N.H. Brook, P.J. Bussey, A.T. Doyle, I. Fleck, V.A. Jamieson, D.H. Saxon, M.L. Utley, A.S. Wilson
Dept. of Physics and Astronomy, University of Glasgow, Glasgow, U.K. [o]

A. Dannemann, U. Holm, D. Horstmann, H. Kammerlocher[8], B. Krebs[9], T. Neumann, R. Sinkus, K. Wick
Hamburg University, I. Institute of Exp. Physics, Hamburg, Federal Republic of Germany [c]

E. Badura, B.D. Burow, A. Fürtjes[10], E. Lohrmann, J. Milewski, M. Nakahata[11], N. Pavel, G. Poelz, W. Schott, J. Terron[7], F. Zetsche
Hamburg University, II. Institute of Exp. Physics, Hamburg, Federal Republic of Germany [c]

T.C. Bacon, R. Beuselinck, I. Butterworth, E. Gallo, V.L. Harris, B.H. Hung, K.R. Long, D.B. Miller, P.P.O. Morawitz, A. Prinias, J.K. Sedgbeer, A.F. Whitfield
Imperial College London, High Energy Nuclear Physics Group, London, U.K. [o]

U. Mallik, E. McCliment, M.Z. Wang, Y. Zhang
University of Iowa, Physics and Astronomy Dept., Iowa City, USA [p]

P. Cloth, D. Filges
Forschungszentrum Jülich, Institut für Kernphysik, Jülich, Federal Republic of Germany

S.H. An, S.M. Hong, S.W. Nam, S.K. Park, M.H. Suh, S.H. Yon
Korea University, Seoul, Korea [h]

R. Imlay, S. Kartik, H.-J. Kim, R.R. McNeil, W. Metcalf, V.K. Nadendla
Louisiana State University, Dept. of Physics and Astronomy, Baton Rouge, LA, USA [p]

F. Barreiro[12], G. Cases, R. Graciani, J.M. Hernández, L. Hervás[12], L. Labarga[12], J. del Peso, J. Puga, J.F. de Trocóniz
Univer. Autónoma Madrid, Depto de Física Teóríca, Madrid, Spain [n]

F. Ikraiam, J.K. Mayer[13], G.R. Smith
University of Manitoba, Dept. of Physics, Winnipeg, Manitoba, Canada [a]

F. Corriveau, D.S. Hanna, J. Hartmann, L.W. Hung, J.N. Lim, C.G. Matthews, J.W. Mitchell[14], P.M. Patel, L.E. Sinclair, D.G. Stairs, M. St.Laurent, R. Ullmann
McGill University, Dept. of Physics, Montreal, Quebec, Canada [a, b]

V. Bashkirov, B.A. Dolgoshein, A. Stifutkin
Moscow Engineering Physics Institute, Mosocw, Russia [l]

G.L. Bashindzhagyan, P.F. Ermolov, L.K. Gladilin, Y.A. Golubkov, V.D. Kobrin, V.A. Kuzmin, A.S. Proskuryakov, A.A. Savin, L.M. Shcheglova, A.N. Solomin, N.P. Zotov
Moscow State University, Institute of Nuclear Pysics, Moscow, Russia [m]

S. Bentvelsen, M. Botje, F. Chlebana, A. Dake, J. Engelen, P. de Jong[15], M. de Kamps, P. Kooijman, A. Kruse, V. O'Dell[16], A. Tenner, H. Tiecke, W. Verkerke, M. Vreeswijk, L. Wiggers, E. de Wolf, R. van Woudenberg
NIKHEF and University of Amsterdam, Netherlands [i]

D. Acosta, B. Bylsma, L.S. Durkin, K. Honscheid, C. Li, T.Y. Ling, K.W. McLean, W.N. Murray, I.H. Park, T.A. Romanowski[17], R. Seidlein
Ohio State University, Physics Department, Columbus, Ohio, USA [p]

D.S. Bailey, G.A. Blair[18], A. Byrne, R.J. Cashmore, A.M. Cooper-Sarkar, D. Daniels[19], R.C.E. Devenish, N. Harnew, M. Lancaster, P.E. Luffman[20], L. Lindemann, J. McFall, C. Nath, A. Quadt, H. Uijterwaal, R. Walczak, F.F. Wilson, T. Yip
Department of Physics, University of Oxford, Oxford, U.K. [o]

G. Abbiendi, A. Bertolin, R. Brugnera, R. Carlin, F. Dal Corso, M. De Giorgi, U. Dosselli, F. Gasparini, S. Limentani, M. Morandin, M. Posocco, L. Stanco, R. Stroili, C. Voci
Dipartimento di Fisica dell' Universita and INFN, Padova, Italy [f]

J. Bulmahn, J.M. Butterworth, R.G. Feild, B.Y. Oh, J.J. Whitmore[21]
Pennsylvania State University, Dept. of Physics, University Park, PA, USA [q]

G. D'Agostini, M. Iori, G. Marini, M. Mattioli, A. Nigro, E. Tassi
Dipartimento di Fisica, Univ. 'La Sapienza' and INFN, Rome, Italy [f]

J.C. Hart, N.A. McCubbin, K. Prytz, T.P. Shah, T.L. Short
Rutherford Appleton Laboratory, Chilton, Didcot, Oxon, U.K. [o]

E. Barberis, N. Cartiglia, T. Dubbs, C. Heusch, M. Van Hook, B. Hubbard, W. Lockman,
J.T. Rahn, H.F.-W. Sadrozinski, A. Seiden
University of California, Santa Cruz, CA, USA [p]

J. Biltzinger, R.J. Seifert, A.H. Walenta, G. Zech
Fachbereich Physik der Universität-Gesamthochschule Siegen, Federal Republic of Germany [c]

H. Abramowicz, G. Briskin, S. Dagan[22], A. Levy[22]
School of Physics, Tel-Aviv University, Tel Aviv, Israel [e]

T. Hasegawa, M. Hazumi, T. Ishii, M. Kuze, S. Mine, Y. Nagasawa, T. Nagira, M. Nakao, I. Suzuki, K. Tokushuku,
S. Yamada, Y. Yamazaki
Institute for Nuclear Study, University of Tokyo, Tokyo, Japan [g]

M. Chiba, R. Hamatsu, T. Hirose, K. Homma, S. Kitamura, S. Nagayama, Y. Nakamitsu
Tokyo Metropolitan University, Dept. of Physics, Tokyo, Japan [g]

R. Cirio, M. Costa, M.I. Ferrero, L. Lamberti, S. Maselli, C. Peroni, R. Sacchi, A. Solano, A. Staiano
Universita di Torino, Dipartimento di Fisica Sperimentale and INFN, Torino, Italy [f]

M. Dardo
II Faculty of Sciences, Torino University and INFN - Alessandria, Italy [f]

D.C. Bailey, D. Bandyopadhyay, F. Benard, M. Brkic, M.B. Crombie, D.M. Gingrich[23], G.F. Hartner, K.K. Joo,
G.M. Levman, J.F. Martin, R.S. Orr, C.R. Sampson, R.J. Teuscher
University of Toronto, Dept. of Physics, Toronto, Ont., Canada [a]

C.D. Catterall, T.W. Jones, P.B. Kaziewicz, J.B. Lane, R.L. Saunders, J. Shulman
University College London, Physics and Astronomy Dept., London, U.K. [o]

K. Blankenship, J. Kochocki, B. Lu, L.W. Mo
Virginia Polytechnic Inst. and State University, Physics Dept., Blacksburg, VA, USA [q]

W. Bogusz, K. Charchuła, J. Ciborowski, J. Gajewski, G. Grzelak, M. Kasprzak, M. Krzyżanowski,
K. Muchorowski, R.J. Nowak, J.M. Pawlak, T. Tymieniecka, A.K. Wróblewski, J.A. Zakrzewski, A.F. Żarnecki
Warsaw University, Institute of Experimental Physics, Warsaw, Poland [j]

M. Adamus
Institute for Nuclear Studies, Warsaw, Poland [j]

Y. Eisenberg[22], C. Glasman, U. Karshon[22], D. Revel[22], A. Shapira
Weizmann Institute, Nuclear Physics Dept., Rehovot, Israel [d]

I. Ali, B. Behrens, S. Dasu, C. Fordham, C. Foudas, A. Goussiou, R.J. Loveless, D.D. Reeder,
S. Silverstein, W.H. Smith
University of Wisconsin, Dept. of Physics, Madison, WI, USA [p]

T. Tsurugai
Meiji Gakuin University, Faculty of General Education, Yokohama, Japan

S. Bhadra[24], W.R. Frisken, K.M. Furutani
York University, Dept. of Physics, North York, Ont., Canada [a]

[1] supported by Worldlab, Lausanne, Switzerland
[2] also at IROE Florence, Italy
[3] now at Univ. of Pisa, Italy
[4] now a self-employed consultant
[5] now at Inst. of Computer Science, Jagellonian Univ., Cracow
[6] now at Univ. of California, Santa Cruz
[7] supported by the European Community
[8] now at DESY
[9] now with Herfurth GmbH, Hamburg
[10] now at CERN
[11] now at Institute for Cosmic Ray Research, University of Tokyo
[12] on leave of absence at DESY, supported by DGICYT
[13] now at Univ. of Toronto
[14] now at Univ. of California, Davis, CA
[15] now at MIT, Cambridge, MA
[16] now at Fermilab., Batavia, IL
[17] now at Department of Energy, Washington
[18] now at RHBNC, Univ. of London, England
[19] Fulbright Scholar 1993-1994
[20] now at Cambridge Consultants, Cambridge, U.K.
[21] on leave and supported by DESY 1993-94
[22] supported by a MINERVA Fellowship
[23] now at Centre for Subatomic Research, Univ.of Alberta, Canada and TRIUMF, Vancouver, Canada
[24] now at DESY

[a] supported by the Natural Sciences and Engineering Research Council of Canada
[b] supported by the FCAR of Quebec, Canada
[c] supported by the German Federal Ministry for Research and Technology (BMFT)
[d] supported by the MINERVA Gesellschaft für Forschung GmbH, and by the Israel Academy of Science
[e] supported by the German Israeli Foundation, and by the Israel Academy of Science
[f] supported by the Italian National Institute for Nuclear Physics (INFN)
[g] supported by the Japanese Ministry of Education, Science and Culture (the Monbusho) and its grants for Scientific Research
[h] supported by the Korean Ministry of Education and Korea Science and Engineering Foundation
[i] supported by the Netherlands Foundation for Research on Matter (FOM)
[j] supported by the Polish State Committee for Scientific Research (grant No. 204209101)
[k] supported by the Polish State Committee for Scientific Research (grant No. PB 861/2/91 and No. 2 2372 9102, grant No. PB 2 2376 9102 and No. PB 2 0092 9101)
[l] partially supported by the German Federal Ministry for Research and Technology (BMFT)
[m] supported by the German Federal Ministry for Research and Technology (BMFT), the Volkswagen Foundation, and the Deutsche Forschungsgemeinschaft
[n] supported by the Spanish Ministry of Education and Science through funds provided by CICYT
[o] supported by the Particle Physics and Astronomy Research Council
[p] supported by the US Department of Energy
[q] supported by the US National Science Foundation

1 Introduction

The first measurements of the proton structure function F_2 in ep neutral current (NC) deep inelastic scattering (DIS) at HERA were reported previously by the H1 and ZEUS collaborations [1, 2]. The large centre of mass energy available at HERA allows measurements to be made for x values as small as 10^{-4} at Q^2 values of the order of 10 GeV^2, at least two orders of magnitude below the lowest values measured in fixed target experiments at this Q^2 [3, 4, 5]. The most striking feature of the data is the strong rise of F_2 as x decreases. There has been much discussion [6] about the significance of this observation both for the standard evolution of structure functions and for the behaviour of the gluon density distribution in the proton at small x.

In this paper we present the measurement of the proton structure function F_2 from the 1993 HERA data with the ZEUS detector. The data sample corresponds to an integrated luminosity of 0.54 pb^{-1} and represents a twenty fold increase over that used in our first measurements. Two independent analyses have been performed, one using our standard double angle (DA) approach and the other based on the energy and angle of the scattered electron. The size of the systematic errors in the DA method has been reduced through the increased statistics and improved understanding of the performance of the detector. In addition to probing to smaller and larger Q^2, the increased data volume allows a finer binning in both x and Q^2.

2 Experimental setup

2.1 HERA machine conditions

The experiment was performed at the electron-proton collider HERA using the ZEUS detector. During 1993 HERA operated with bunches of electrons of energy $E_e = 26.7$ GeV colliding with bunches of protons of energy $E_p = 820$ GeV, with a time between bunch crossings of 96 ns. HERA is designed to run with 210 bunches in each of the electron and proton rings. For the 1993 data taking 84 paired bunches were filled for each beam and in addition 10 electron and 6 proton bunches were left unpaired for background studies. The electron and proton beam currents were typically 10 mA. For most of the data taken in 1993 the HERA proton ring RF frequency was 208 MHz which gave a root mean square proton bunch length of about ± 20 cm.

2.2 The ZEUS detector

ZEUS is a multipurpose magnetic detector that has been described elsewhere [7, 8]. Here we give a brief description of those parts of the detector relevant for the present analysis.

Charged particles are tracked by the inner tracking detectors which operate in a magnetic field of 1.43 T provided by a thin superconducting coil. Immediately surrounding the beampipe is the vertex detector (VXD), a cylindrical drift chamber, which consists of 120 radial cells, each with 12 sense wires. It uses a slow drift velocity gas (dimethylether)[9] and the presently achieved resolution is 50 μm in the central region of a cell and 150 μm near the edges. Surrounding the VXD is the central tracking detector (CTD) which consists of 72 cylindrical drift chamber layers, organised into 9 'superlayers' [10]. With the present understanding of the chamber, a spatial resolution of $\sim$ 260 μm has been achieved. The resolution in transverse momentum for full length tracks is $\sigma_{p_T}/p_T = 0.005 p_T \oplus 0.016$ (for p_T in GeV).

The solenoid is surrounded by a high resolution uranium-scintillator calorimeter (CAL) di-

vided into three parts, forward (FCAL) covering the pseudorapidity[1] region $4.3 \geq \eta \geq 1.1$, barrel (BCAL) covering the central region $1.1 \geq \eta \geq -0.75$ and rear (RCAL) covering the backward region $-0.75 \geq \eta \geq -3.8$. Holes of 20×20 cm^2 in the centre of FCAL and RCAL are required to accommodate the HERA beam pipe. The resulting solid angle coverage is 99.7% of 4π. The calorimeter parts are subdivided into towers which in turn are subdivided longitudinally into electromagnetic (EMC) and hadronic (HAC) sections. The sections are subdivided into cells, each of which is viewed by two photomultiplier tubes. Under test beam conditions the CAL has an energy resolution, in units of GeV, of $\sigma_E = 0.35\sqrt{E(\mathrm{GeV})}$ for hadrons and $\sigma_E = 0.18\sqrt{E(\mathrm{GeV})}$ for electrons. The CAL also provides a time resolution of better than 1 ns for energy deposits greater than 4.5 GeV, which is used for background rejection. For the 1993 data taking most of the RCAL was instrumented with the hadron-electron separator (HES), consisting of an array of 3×3.2 cm^2 silicon diodes located at a depth of 3.3 radiation lengths (r.l.). The calorimeter is described in detail in [11, 12, 13].

The C5 beam monitor, a small lead-scintillator counter, located[2] at $Z = -3.2$ m was used to detect upstream proton beam interactions and to measure the timing and longitudinal structure of the proton and electron bunches. The vetowall detector, consisting of two layers of scintillator on either side of an 87 cm thick iron wall centered at $Z = -7.3$ m was also used to tag off-beam background particles.

For measuring the luminosity as well as for tagging very small Q^2 processes, we use two lead-scintillator calorimeters [14]. Bremsstrahlung photons emerging from the electron-proton interaction point (IP) at angles $\theta_\gamma \leq 0.5$ mrad with respect to the electron beam axis hit the photon calorimeter at 107 m from the IP. Electrons emitted from the IP at scattering angles less than or equal to 6 mrad and with energies $0.2E_e < E'_e < 0.9E_e$ are deflected by beam magnets and hit the electron calorimeter placed 35 m from the IP.

2.3 Trigger conditions

Data were collected with a three level trigger [7]. The First Level Trigger (FLT) is built as a deadtime-free pipeline. The FLT for DIS events required a logical OR of three conditions on sums of energy in the EMC calorimeter cells: either the BCAL EMC energy exceeded 3.4 GeV; or the RCAL EMC energy, excluding the towers immediately adjacent to the beam-pipe, exceeded 2.0 GeV; or the RCAL EMC energy, including the beam-pipe towers, exceeded 3.75 GeV. In addition, an alternative high transverse energy trigger included DIS events with electrons in the FCAL. For events with the scattered electron detected in the calorimeter, the FLT was essentially independent of the DIS hadronic final state. The FLT acceptance was 95% at $Q^2 = 5$ GeV^2 rising to a constant value close to 100% for $Q^2 > 10$ GeV^2. The hardware inefficiency of the DIS FLT due to dead channels and calibration errors was found to be at most 1% from a study of independent triggers.

The Second Level Trigger (SLT) used information from a subset of detector components to differentiate physics events from backgrounds. The SLT rejected proton beam-gas events using the event times measured in the RCAL thereby reducing the FLT DIS triggers by an order of magnitude, but without loss of DIS events.

The Third Level Trigger (TLT) had available the full event information on which to apply

[1] The pseudorapidity η is defined as $-\ln(\tan\frac{\theta}{2})$, where the polar angle θ is taken with respect to the proton beam direction from the nominal interaction point.

[2] The ZEUS coordinate system is defined as right handed with the Z axis pointing in the proton beam direction, hereafter referred to as forward, and the X axis horizontal, pointing towards the centre of HERA.

physics-based filters. The TLT applied stricter cuts on the event times and also rejected beam-halo muons and cosmic muons. Events remaining after these cuts were selected for output by the TLT if

$$\delta \equiv \Sigma_i E_i(1-\cos\theta_i) > 20\text{GeV} - 2E_\gamma \tag{1}$$

where E_i, θ_i are the energy and polar angle (with respect to the nominal IP) of calorimeter cells and E_γ is the energy measured in the photon calorimeter of the luminosity monitor. For fully contained events $\delta \sim 2E_e = 53.4$ GeV. For events from photoproduction processes δ peaks at low values; this is because the scattered electrons remain within the rear beam pipe and the bremsstrahlung spectrum is soft.

The overall trigger acceptance after all three levels is above 95% independent of x and Q^2 in the ranges of interest for this analysis.

2.4 Luminosity measurement

The luminosity is measured from the rate observed in the luminosity gamma detector of hard bremsstrahlung photons from the Bethe-Heitler process $ep \to e'p\gamma$. The background rate from electron beam bremsstrahlung on the residual gas in the beampipe was subtracted using the unpaired electron bunches. More details on the method are given in [14, 15, 16]. The longitudinal structure of the beams was measured from C5 timing signals and from the reconstructed primary vertices in non-diffractive photoproduction events. Approximately 3% of the proton current was contained in satellite bunches which resulted in interactions at $Z = +60$ cm from the nominal IP. The acceptance of the luminosity monitor does not depend on the proton bunch timing and so includes both the main and proton satellite peaks.

The overall systematic error on the integrated luminosity for the 1993 data is 3.3%, the largest contributions coming from the acceptance correction and the photon calorimeter energy calibration.

3 Kinematics

In deep inelastic scattering

$$e(k) + p(P) \to e'(k') + anything$$

the structure functions are expressed as functions of Bjorken x and Q^2, the negative of the four-momentum transfer squared. The basic quantities, in the absence of QED radiation at the electron vertex, are:

$$Q^2 = -q^2 = -(k-k')^2 \tag{2}$$

$$x = \frac{Q^2}{2P\cdot q} \tag{3}$$

$$y = \frac{P\cdot q}{P\cdot k} \tag{4}$$

where k and k' are the four-momenta of the initial and final state electrons, P is the initial state proton four-momentum, and y is the fractional energy transfer to the proton in its rest frame.

Because the ZEUS detector is almost hermetic the kinematic variables x and Q^2 can be reconstructed in a variety of ways using combinations of electron and hadronic system energies and angles [17]. The ability to measure x and Q^2 in different ways offers a powerful systematic check on the resulting F_2 values. In this paper we use two methods:

1. the classic electron method in which the kinematic variables are reconstructed from the energy (E'_e) and angle (θ'_e) of the scattered electron;

2. the DA method in which only the angles of the scattered electron (θ'_e) and the hadronic system (γ_H) are used, which reduces the sensitivity to energy scale uncertainties. The angle γ_H is that of a massless object balancing the momentum vector of the electron to satisfy four-momentum conservation. In the naïve quark-parton model γ_H is the scattering angle of the struck quark. It is determined from the hadronic energy flow measured in the detector using the equation

$$\cos\gamma_H = \frac{(\sum_h p_{\rm X})^2 + (\sum_h p_{\rm Y})^2 - (\sum_h (E - p_{\rm Z}))^2}{(\sum_h p_{\rm X})^2 + (\sum_h p_{\rm Y})^2 + (\sum_h (E - p_{\rm Z}))^2} \tag{5}$$

   where the sums, $\sum_h$, run over all calorimeter cells h which are not assigned to the scattered electron, and $(p_{\rm X}, p_{\rm Y}, p_{\rm Z})$ is the momentum vector assigned to each cell of energy E. The cell angles are calculated from the geometric centre of the cell and the vertex position of the event.

Method 1 gives better resolution in x at low Q^2 and method 2 is less sensitive to the calorimeter energy scale and gives the better mean resolution over the whole x–Q^2 plane. Complete formulae for calculating the variables x, y and Q^2 are to be found in [17]. When it is necessary to distinguish which method has been used the subscripts 'e' or 'DA' will be used on the variable concerned.

In the double angle method in order that the hadronic system be well measured it is necessary to require a minimum of hadronic activity in the CAL away from the beampipe. A suitable quantity for this purpose is the hadronic estimator of the variable y [18], defined by

$$y_{JB} = \frac{\sum_h (E - p_{\rm Z})}{2E_e} \tag{6}$$

where E_e is the electron beam energy.

4 Monte Carlo simulation

Monte Carlo event simulation is used to correct for acceptance and resolution effects. The detector simulation is based on the GEANT [19] program and incorporates knowledge of the apparatus, test beam results and trigger. More details of the detector (MOZART) and trigger (ZGANA) simulation codes are given in [7].

Neutral current DIS events with $Q^2 > 4\,{\rm GeV}^2$ were generated using the HERACLES [20] program, which includes first order electroweak radiative corrections. The hadronic final state was simulated using the color-dipole model [21] including boson gluon fusion as implemented in ARIADNE [22] for the QCD cascade, and JETSET [23] for the hadronisation. The ARIADNE model gives the best overall description of our observed energy flow and other final state properties and is used for the standard corrections and unfolding of F_2. The default parameterisation of the parton distribution functions (PDFs) is the MRSD'_ set [24] but we also use the

$MRSD'_0$, CTEQ2D′ [25] and GRV(HO) [26] sets. To check event migration at the lowest values of Q^2 a sample of ARIADNE events with $Q^2 > 2\,\mathrm{GeV}^2$ and the GRV(HO) structure is used. To study the sensitivity of resolution and acceptance corrections to models of the final state and fragmentation, a sample of DIS events was also generated using LEPTO (MEPS option) [27].

As we explain in more detail in Section 8.2.1 below, the data sample contains a contribution ($\sim$ 10%) from events with a large rapidity gap (LRG) in the hadronic final state [28, 29]. These events are not simulated in the above Monte Carlo programs. Separate Monte Carlo event samples were produced using POMPYT [30] (with a hard parton momentum density in the pomeron) and the Nikolaev-Zakharov (NZ) [31] models, both of which give reasonable descriptions of the properties of LRG events [29]. These samples are used to check acceptance and event migrations. They do not contain QED radiative processes.

The main source of background in the DIS sample is photoproduction at high y, in which a fake electron signal is produced either by a photon or by a charge exchange interaction in the detector material. To study this, we generated events with $Q^2 < 2$ GeV^2 using the PYTHIA [32] program. The spectrum of scattered electrons was generated down to $Q^2 = 0$ using the ALLM parameterisation [33] of the total photoproduction cross section. The hadronic final state was simulated in the $\gamma^* p$ centre of mass system using the multiparton interaction scheme [34] implemented in PYTHIA for hadron–hadron scattering.

To determine the acceptance of the trigger and data selection, the Monte Carlo events were passed through the reconstruction and selection procedures identical to those for the data described in the next section. The large ARIADNE sample used for correction and unfolding corresponds to an equivalent integrated luminosity of 738 nb^{-1}.

5 Event selection

5.1 General remarks

In the 1993 data taking a total of 2×10^6 events was recorded with the DIS trigger described in Section 2.3. Events were reconstructed with the ZEUS reconstruction program ZEPHYR [7]. After reconstruction and a filter requiring a loosely defined electron with $E'_e > 4$ GeV, and a cut on δ as in equation (1) but with 20 GeV raised to 25 GeV, 3.1×10^5 events remained. The event selection procedure is designed to recognise events with a scattered beam electron and to remove remaining beam-gas and cosmic ray backgrounds. The cuts also control the magnitude of radiative corrections and minimise contamination of the DIS sample by mis-identified photoproduction events. Electrons are recognised by the spatial pattern of energy deposition in the CAL and by the ratio of EMC to HAC energies. By adjusting the parameters of the algorithm the purity and efficiency can be tuned to the particular physics goal. For the standard F_2 analysis we tune the electron finder for high purity. From studies with the ARIADNE Monte Carlo sample the electron finding efficiency is found to average 95% in the $x - Q^2$ bins used to measure F_2, being above 98% in most bins and only dropping below 70% in two edge bins at high y. The purity is better than 97% for energies above 12 GeV. For systematic checks we use a neural network electron finder [35], which is very different from the above cone-based algorithm, but has similar electron finding efficiency and purity.

The primary event vertex is determined from tracks reconstructed using VXD+CTD information. The resolution of the Z-coordinate of the primary vertex, Z_{vtx}, has been investigated by comparing the results of two different track reconstruction codes and from Monte Carlo simulation. The mean resolution of Z_{vtx} is 0.4 cm for the entire region in x and Q^2 used for

the F_2 analysis. Figure 1 shows the Z_{vtx} distribution for DIS data (solid points) and for the Monte Carlo events (histogram), normalised to the number of data events. The Monte Carlo events were generated with a Z_{vtx} distribution determined from non-diffractive photoproduction events. Data and Monte Carlo are in good agreement. The figure also shows that the proton satellite peak at +60 cm is well described. A gaussian fit to the main peak has a root mean square width of $\pm$10.4 cm. If no tracking information is available Z_{vtx} is estimated from FCAL timing [2], with a resolution of 10.2 cm. If neither tracking nor FCAL timing is present the vertex position is set to the nominal IP. In the DA DIS sample we find that 99% events have a good tracking vertex in agreement with the ARIADNE Monte Carlo simulation, 0.6% have only a FCAL timing vertex and 0.4% neither. In the electron analysis 91% of events have a tracking vertex, with a corresponding figure of 93% in the simulation. A larger fraction of events do not have a tracking vertex because the y_{JB} cut (see below) is not applied.

The impact point of the electron on the CAL face is measured using the energy sharing between the two phototubes that view each cell and the energy sharing between neighbouring cells among the cells assigned to the electron. The typical resolution is 1 cm, except close to the beam pipe [2]. The shorter proton bunch length in the 1993 run and the vertex resolution improvement from the fully instrumented CTD together lead to a better determination of the electron scattering angle. The electron angular resolution is better than 0.1° except for angles above 165° when it rises to 0.25°. The angular resolution of γ_H is much the same as it was for the 1992 analysis and is 16° at $y_{JB} = 0.04$ improving to 12° for $y_{JB} \geq 0.1$. Below y_{JB} of 0.02 the measurement of γ_H is distorted by noise in the calorimeter.

5.2 Double angle method

In detail the DA DIS sample must satisfy the following criteria, where the number in brackets following each cut is the number of events surviving that cut:

- $E'_e > 5$ GeV - to have reliable electron finding and to control the photoproduction background (181k);
- $|t_R| < 6$ ns and $|t_F - t_R| < 6$ ns - to reject beam related backgrounds and cosmic rays, where t_R and t_F are the mean times recorded in the RCAL and FCAL [36] (180k);
- $y_e < 0.95$ - to reject photoproduction background (179k);
- the impact point of the electron on the face of the RCAL lies outside a square of side 32 cm centered on the beam axis (box cut) - to ensure full containment of the electron shower (92k) ;
- $y_{JB} > 0.04$ - to ensure a good measurement of the angle γ_H and x (58k);
- $35 < \delta < 60$ GeV (where δ is defined by equation (1) but now with angles referred to the event vertex) - to control radiative corrections and reduce photoproduction background (46.4k).

After the selection cuts, and the removal of 172 QED Compton scattering events, 125 residual cosmic-ray events and 100 events from non-colliding bunches, the DA DIS sample contains 46k events corresponding to an integrated luminosity of 543 nb^{-1}.

Figure 2a shows the y_{JB} distribution, integrated over $Q^2 > 7$ GeV^2 but before the cut on y_{JB} is applied, for the data (solid circles) together with the expectation from the ARIADNE

simulation with MRSD'_ PDFs (histogram). The shape of the simulated y_{JB} distribution is quite sensitive to the details of the fragmentation model, the input PDFs and the modelling of the CAL response. It is difficult to isolate these effects and we have not been able to obtain a completely satisfactory description of this distribution. However one of the largest effects is the input PDF and it can be seen from Figure 2b that reweighting the ARIADNE simulation to the measured ZEUS F_2 improves considerably the description of the data. It should be noted that y_{JB} is used as a selection cut, but it does not enter directly in the calculation of the kinematic variables in the DA method.

5.3 Electron method

5.3.1 Electron energy correction

In the ZEUS detector the primary tool for electron identification and measurement is the uranium-scintillator calorimeter. The absolute calibration of the CAL has been determined by test beam measurements [11, 12] and is maintained by monitoring the level of the natural uranium radioactivity. The calibration is estimated to be correct to better than 2% and has been checked using beam halo muons [37]. However scattered DIS electrons in ZEUS typically pass through 1 r.l. (rising to as much as 6 r.l. in certain regions) of material before reaching the CAL. If x and Q^2 are to be reconstructed from the electron's angle and energy it is necessary to correct the measured energy for energy loss in the inactive material. Using the large 1993 data sample the correction can be determined in a direct way. At low values of y the scattered electron energy deviates very little from the incident beam energy of 26.7 GeV, independently of x and Q^2, giving rise to the so called kinematic peak (KP). KP events are selected by requiring the standard DA DIS cuts with the exception of the y_{JB} cut ($y_{JB} > 0.04$) which is replaced by $y_{JB} < 0.03$ and also requiring $Q^2_{DA} < 100$ GeV^2. Figure 3 shows the KP area in the $x - Q^2$ plane. Note that with these cuts the KP sample does not overlap that used for the DA F_2 analysis. The position of the kinematic peak does not depend on the value of F_2, and this has been checked in the Monte Carlo data using MRSD'_ , MRSD$'_0$ and CTEQ2D$'$ PDFs.

The principle of the method is to use the KP electrons to measure the energy loss in inactive material in front of the RCAL. Bins on the face of the RCAL are chosen so that in a given bin the electrons traverse a roughly constant amount of material before reaching the detector. In practice the choice of bin size is also limited by statistics. The observed shift of the KP electron energy from E_e in a bin is then compared to test beam data[3] with known amounts of absorber before the CAL modules to produce a map of inactive material depth in front of the RCAL. Electron energy loss as a function of material depth in units of r.l. and E'_e from test beam data are used to calculate the energy loss for electrons in the RCAL. The same procedure is applied to Monte Carlo data. The correction functions have been determined for electron impact points on the RCAL face within a circle of radius 60 cm centered on the rear beam direction. After correction the positions of the KP in data and simulation agree to about 1% at the expected value of 26.7 GeV. The correction functions for data and Monte Carlo are different because the ZEUS detector simulation code is not yet quite accurate enough in its description of material in the backward region near the rear beam pipe and this affects particularly the electron electromagnetic shower simulation. The difference, which is presently not completely understood, is compatible with the hypothesis that about 1 r.l. of inactive material is missing in the simulation in the angular range $167° < \theta'_e < 174°$.

[3]The test beam data were recorded without a magnetic field.

We have used three independent physics channels to verify that the RCAL electron energy correction is accurate to about the 1% level.

- Elastic QED Compton scattering events have a final state consisting of an electron and a photon. For Compton events the sum of the electron and gamma energies should satisfy, to a good approximation,

$$E_1 + E_2 = E_e + M^2_{e\gamma}/(4E_e) \tag{7}$$

  where $M_{e\gamma}$ is the $e\gamma$ invariant mass. Using energy and momentum conservation, $M_{e\gamma}$ is calculated from the angles of the electron and photon measured in the CAL. The scale on the r.h.s. of equation (7) is set by the electron beam energy so the ratio of the measured quantity $E_1 + E_2$ to the r.h.s. of the equation gives a direct check on the energy loss correction. Using 149 selected Compton events[4] and uncorrected energies we find a mean of 0.88 for the ratio and using corrected energies a value of 1.01.

- In diffractive DIS ρ events the ρ^0 is the hadronic final state and its contribution to δ can be calculated to an accuracy of 1% from charged particle track information. The scattering angle of the electron is measured in the usual way from CAL information. Using energy and momentum conservation an estimate of E'_e is obtained independently of the RCAL energy scale. From a sample of 193 DIS ρ events the mean of the ratio $E'_e(\mathrm{RCAL})/\mathrm{E'_e}(\rho)$ is found to be 0.84 without the RCAL energy loss correction and 0.99 with it.

- DIS events in which a hard initial state radiative photon is measured in the luminosity gamma detector can also be used to check the RCAL energy, corrected for the loss in the inactive material, against that of the luminosity gamma detector. This method is slightly less accurate than the other two but from a sample of about 1000 such events the corrected RCAL energies agree, within the expected uncertainty of 2%, with those predicted by the luminosity gamma detector.

5.3.2 Electron data selection

For the electron method the event selection procedure is very similar to that described in Section 5.2 above for the DA method, except that the electron energy is corrected before the E'_e, y_e and δ cuts are applied. In detail the cuts are, where the number in brackets following each cut is the number of events surviving that cut:

- E'_e(corrected)$>$ 8 GeV (154k);
- $|t_R| < 6$ ns and $|t_F - t_R| < 6$ ns (153k);
- $y_{el} < 0.95$ (152.5k);
- the impact point of the electron on the face of the RCAL lies outside a square of side 32 cm centered on the beam axis (66.1k);
- $35 < \delta < 65$ GeV - the upper cut is at 65 rather than 60 GeV because the corrected electron energy shifts the peak of the δ distribution to a higher energy (58.2k);

[4]The cuts used here to select Compton events are more restrictive than those used in Section 5.2 to reject QED Compton background.

- the electron impact point on the RCAL face must lie within a circle of radius 60 cm centered on the beam axis (which corresponds to a maximum Q^2 of roughly 100 GeV^2) (53.6k).

After these cuts, and the removal of QED Compton events and cosmic-ray events, the electron DIS sample contains 52.5k events. Note that no cut on y_{JB} is applied.

6 Choice of bins and data characteristics

6.1 Choice of bins in x and Q^2

Figure 4 shows the distribution in the $x - Q^2$ plane of the DA DIS event sample. Lines of constant $y = 1$ (full - kinematic boundary) and $y = 0.04$ (dashed) are shown as well as the region covered by fixed target experiments. The accessible kinematic region is limited at low Q^2 by the box cut and at high Q^2 by statistics. In x, at fixed Q^2, the kinematic region is bounded on the high y side by the cut on y_e and the cut on the electron energy (at low Q^2 values). At low y the boundary comes from the cut on y_{JB} in the DA method. In the electron method, for $Q^2 < 100$ GeV^2, the limit at low y comes from the poor x resolution of the KP region.

F_2 is a function of x and Q^2 and in order to measure it the data are binned in these variables. Bins are chosen commensurate with the resolutions in x and Q^2. At high Q^2 limited statistics determines the size of bins. Full details are given in Table 1 for the low Q^2 bins and in Table 2 for the high Q^2 bins. For both the DA and electron methods the relative resolution in Q^2 is 25% independent of Q^2, so we can use the same Q^2 binning for both methods (for the electron method only bins below 80 GeV^2 are relevant). For the DA method the relative x resolution varies smoothly with x from 20% at 10^{-2} to 50% at 10^{-3} and is almost independent of Q^2. In principle using the electron method the x resolution should improve at low values of x. However, although the electron energy is corrected for energy loss in the inactive material, the degradation in energy resolution cannot be completely recovered. As the net improvement in x resolution is rather small we use the same binning in x as for the DA method.

Not all bins compatible with the resolution are used in the analysis. The most important factor in the choice of bins is the overall acceptance after all cuts. Figure 5 shows the acceptance in the chosen bins and it can be seen that it is well above 80% in most bins. In only two bins at low Q^2 does the acceptance drop below 60%. Other factors must also be taken into account: purity (the fraction of simulated events generated in a bin and measured in the same bin) must be above 30% and is in fact above 45% in most bins; at high Q^2 the minimum number of events in a bin is required to be 10. Together these considerations lead to the choice of 'selected' bins shown for the DA method in Figure 4. For the DA analysis a total of 37k events remain in the selected bins and for the electron analysis a total of 35.7k events lie in the bins with $Q^2 < 80$ GeV^2.

6.2 Kinematic distributions

In this section the kinematic properties of the two DIS samples in the selected bins are described and compared to the ARIADNE simulation.

For the DA DIS sample Figures 6a and b show the primary measured quantities, θ'_e and γ_H respectively. In both plots the data is represented by the solid circles and the ARIADNE simulation, adjusted to the measured F_2, by the histograms. The distributions of both angles

are generally well described by the simulation, except for a small excess in the data at large angles (near the rear beam pipe). The problems that were encountered in the exact description of the y_{JB} distribution do not affect that of γ_H. The variables Q^2_{DA} and x_{DA}, calculated from θ'_e and γ_H, are shown in Figures 6c and d respectively. The agreement between the data and the Monte Carlo simulation is good. For all the plots of Figure 6, the simulation has been reweighted to the measured F_2 and normalised to the number of data events. Also note that the residual photoproduction and other background events have not been subtracted from the data.

In the electron analysis the kinematic variables are calculated after the appropriate electron energy corrections have been applied to the data and Monte Carlo events. Figures 7a and b, for the electron DIS sample, show the distributions of E'_e and θ'_e respectively. In both, the data (solid circles) is well described by the ARIADNE simulation (histograms). In particular the good agreement between the shapes of the E'_e distributions is another confirmation of the correctness of the RCAL energy loss corrections. Figures 7c and d show the distributions of x_e and Q^2_e calculated from E'_e and θ'_e. In both cases the description of the data by the simulation is good. As in the case of the DA analysis, the ARIADNE simulation has been reweighted to the measured F_2 and normalised to the number of data events and background events have not been subtracted from the data.

The good agreement between the ARIADNE simulation and the data for the kinematic variable distributions for both methods shown in Figures 6 and 7 shows the consistency of our correction and unfolding procedure.

7 Backgrounds

7.1 Non-ep backgrounds

The level of beam gas background is estimated by using the numbers of events passing the DIS selection cuts from the unpaired electron and proton bunches, scaled by the ratio of bunch currents. For proton beam-gas we find a level of less than 0.1% and for electron beam-gas a level of at most 0.8%. Figure 8 shows, on a log scale, the contribution from beam-gas background (open squares) to the measured δ distribution. The contamination by cosmic ray events in the final sample is estimated from the empty bunches to be less than 0.05%. These backgrounds are subtracted statistically. If a vertex cut is applied the non-ep backgrounds are reduced to a negligible level.

7.2 ep backgrounds

The most serious residual background in the DIS sample is that from photoproduction. Figure 8 shows the δ spectrum for the DA sample (triangles), together with tagged[5] photoproduction data (filled circles). The figure shows that δ has a minimum in the region of 35 GeV between the falling background distribution (mainly determined by the shape of the bremsstrahlung spectrum) and the rising edge of the peak in δ from DIS events. This is the reason for the standard value of the lower cut on δ being set at 35 GeV. Two methods have been used to estimate the level of photoproduction background in each bin:

[5]The scattered electron was recorded in the luminosity electron detector.

1. For the electron method the δ distribution of photoproduction events was generated with the PYTHIA Monte Carlo and passed through the complete reconstruction and DIS selection procedure.

2. For the DA analysis, in each bin a combination of exponential and gaussian curves is fit to the shape of the measured δ distribution (before the cut on δ is applied) from which the background level is estimated. An example of the method for one $x - Q^2$ bin is shown in Figure 9. The description of the overall δ distribution and background by these functional forms is shown in Figure 8 by the full and dash-dotted curves respectively.

The photoproduction background is not distributed uniformly over the $x - Q^2$ plane; it reaches up to 12% at high y (low E'_e), but for most bins it amounts to only a few percent. As the two methods of estimating the background agree with each other to within 50%, an error of 50% is assigned to the level of photoproduction background subtracted from the data. In addition the background level is sensitive to the cut on the electron energy and the details of the electron finder algorithm. These points will be considered again in Section 8.2 where systematic uncertainties are discussed.

7.3 Upper limits on backgrounds

In some bins, using the methods outlined above, the background is found to be zero. For the Q^2 bins at 500 GeV^2 and above the DA DIS event sample was scanned and no non-ep events (beam-gas and cosmic ray) were found. For the other bins an upper limit is calculated at a confidence level of 68% using Poisson statistics. In some of these bins at large x, given the DA event selection cuts $E'_e > 5$ GeV and $y_e < 0.95$, contributions from beam-gas interactions are kinematically impossible. In these bins the upper limit is 3 events determined from the level of cosmic-ray background events. In the remaining bins the upper limit is 14 events, determined from all non-ep sources. The numbers quoted are after scaling up by the appropriate ratios of bunch currents or bunch numbers. The limits for the DA analysis are given in Tables 1 and 2, but in all cases no events were subtracted from the data in these bins. A similar approach was taken in the electron analysis.

8 The proton structure function F_2

8.1 Extraction

In deep inelastic scattering the double differential cross section for inclusive ep scattering mediated by virtual photon and Z^0 exchanges is given in terms of the structure functions $\mathcal{F}_i$ by:

$$\frac{d^2\sigma}{dx\,dQ^2} = \frac{2\pi\alpha^2}{xQ^4}\left[Y_+\mathcal{F}_2(x,Q^2) - y^2\mathcal{F}_L(x,Q^2) + Y_-x\mathcal{F}_3(x,Q^2)\right](1+\delta_r(x,Q^2)) \qquad (8)$$

where $Y_\pm = 1 \pm (1-y)^2$ and x and Q^2 are defined at the hadronic vertex of the scattering amplitude. $\mathcal{F}_L$ is the longitudinal structure function, $\mathcal{F}_3$ the parity violating term arising from Z^0 exchange and δ_r the radiative correction. We denote by $F_2(x,Q^2)$ and $F_L(x,Q^2)$ the familiar ep structure functions containing contributions from the exchange of a virtual photon only. In this analysis we extract F_2 as explained below. At the highest mean Q^2 of 4200 GeV^2 in the

selected bins the contribution from Z^0 exchange to the cross section is equivalent to a 20% correction to F_2. This has been calculated using the MRSD'_ PDFs and GLAP [38] evolution. For the next lowest Q^2 bin the Z^0 corrections are already less than 6%. We must also correct for F_L, particularly in the small x (high y) bins at low Q^2 where it can amount to a 12-15% correction. The F_L correction factors, calculated using the QCD expectation [39] with the MRSD'_ PDFs, are given in Tables 1 and 2.

According to the HERACLES simulation, using the DA method and a cut on δ of 35 GeV (equivalent to a cut of 9 GeV on the unseen photon in the case of initial state radiation), radiative corrections are in the range $3-5\%$ for $x < 10^{-2}$. These results are in agreement with the recent calculations by Blümlein [40] for the DA method. We have checked the reliability of the radiative corrections with a sample of DIS events in which a hard initial state radiative photon was recorded in the luminosity photon detector. Figure 10 shows a comparison of the differential cross section in bins of E_γ from the data with an absolute prediction of the HERACLES Monte Carlo code for $Q_h^2 > 4$ GeV^2, confined to a region of E_γ where the background from quasi-elastic $ep \to ep\gamma$ events is less than 1%. (Q_h^2 is the value of Q^2 calculated at the hadron vertex.) The agreement between the data and Monte Carlo simulation in both shape and normalisation is good. In the case of the electron method the radiative corrections are at most 10% in the bins with Q^2 up to 80 GeV^2 where the method is used.

Since the Z^0, F_L and radiative corrections are small in all bins we can rewrite equation (8) as

$$\frac{d^2\sigma}{dx\,dQ^2} = \frac{2\pi\alpha^2 Y_+}{xQ^4} F_2(x,Q^2)(1-\delta_{F_L}+\delta_Z)(1+\delta_r) \tag{9}$$

with an obvious notation, and where the corrections $\delta_{F_L,Z,r}$ are functions of x and Q^2 but, to a good approximation, independent of F_2.

To unfold the effect of acceptance, event migration and the δ_i corrections we use the ARIADNE and HERACLES Monte Carlo event sample which was generated according to equation (8) and thus contains transverse and longitudinal photon and Z^0 contributions and radiative effects. There are many ways in which the corrected F_2 can be obtained, for example by correcting back to the Born cross section and then removing $\mathcal{F}_L$ and $\mathcal{F}_3$. For both analyses we unfold directly back to the virtual photon F_2 by using equation (9), which is accurate if the δ_i corrections are small and do not depend strongly on F_2. From the ARIADNE Monte Carlo events a bin-by-bin overall acceptance and correction matrix is calculated, relating the generated number of events in a bin to the 'measured' number in the simulation. The essence of the unfolding method [41] is to modify the starting F_2 iteratively until the distribution of 'measured' Monte Carlo events in the selected bins matches that of the data, making due allowance for the ratio of the data luminosity to that corresponding to the total number of Monte Carlo events. Starting from F_2 calculated using the MRSD'_ PDFs and using some smoothing of the unfolded Monte Carlo data after each iteration, typically 2 or 3 iterations are needed. More than one unfolding method has been used and the methods have been tested by using as 'data' Monte Carlo events weighted with PDFs different from the standard MRSD'_ . The same procedure is used to unfold F_2 in both the DA and electron analyses, applying the appropriate selection cuts to define the 'measured' Monte Carlo sample in each case. The statistical error contains the error from the number of events in data and simulation and the error from the photoproduction background subtraction all added in quadrature.

8.2 Systematic errors

Before we discuss the systematic errors of each method, we consider some problems associated with the hadronic final state simulation which mainly affect the DA method.

8.2.1 Simulation of the hadronic final state

As we have reported in [29] about 8-10% of the DIS events contain a large rapidity gap. These events cannot be accounted for by the standard ARIADNE Monte Carlo simulation. We define η_{max} as the maximum pseudorapidity of all calorimeter clusters in an event, where a cluster is defined as an isolated set of adjacent cells with summed energy above 400 MeV. The DIS events with $\eta_{max} < 1.5$ constitute the large rapidity gap (LRG) sample. The LRG events have been shown to be consistent with a leading twist diffractive production mechanism [28, 29] and their properties can be adequately described by the diffractive Monte Carlo models referred to in Section 4. We have used event samples from the diffractive simulations to check that the kinematic properties and event migrations of the LRG events are close enough to those of the standard DIS events that we can use the ARIADNE Monte Carlo to unfold the total sample without serious error. However, as the diffractive events are missing in the ARIADNE Monte Carlo sample, we have also used a mixture of 90% ARIADNE and 10% POMPYT (or NZ events), which gives a reasonable account of the η_{max} distribution in DIS events [29], to unfold F_2. The resulting changes to the F_2 values constitute one source of the systematic error to be discussed below.

Although the ARIADNE Monte Carlo simulation gives a good description of the DIS hadronic final state the sensitivity of the correction and unfolding procedure to the final state model needs to be checked. For this purpose we use the MEPS Monte Carlo which provides a reasonable description of the final state but does not describe the hadronic energy flow quite as well as ARIADNE [42]. Using MEPS to unfold F_2, we find values well within the DA systematic errors described below, which shows that the correction and unfolding procedure is not very sensitive to the details of the final state model.

8.2.2 DA method systematic errors

We have made many checks on the stability of the DA measurement of F_2. In each case a change is made to one aspect of the analysis and the full evaluation of F_2 repeated. The bin-by-bin changes in F_2 from the standard central values are recorded. To evaluate the overall systematic error we have considered in turn the essential ingredients in the analysis. In detail the systematic error is calculated from the following changes and each one is numbered for later reference.

- Errors associated with electron finding and background subtraction. As we mentioned in Section 7.2 the level of photoproduction background depends on the details of the electron finding algorithm. To check the sensitivity to the electron finder algorithm and photoproduction background, the neural net electron finder was used (1). The largest changes to F_2 (10%) occur in the bins on the high y side of the selected region.

- Below electron energies of 15 GeV the electron finding efficiency may be affected by a slight mismatch between data and Monte Carlo in the pattern of energy deposition. Based on test-beam and Monte Carlo studies we have modified the electron finding efficiency to account for this difference. The largest change to F_2 is less than 5% (2).

- Electron energy scale. Although the DA reconstruction does not depend directly on the electron energy scale, the selection cuts do. To check this we have repeated the DA analysis using corrected electron energies throughout (3). For most bins the change is a few percent but in two high y bins it is 12 and 17%, respectively.

- Electron angle. The electron angle is calculated from the impact position on the CAL face and the primary vertex position. The region where we are most sensitive to the position uncertainty is near to the RCAL beam-pipe hole, which corresponds to low Q^2. To estimate the systematic error we make two changes: vary the box cut from the standard square box of side 32 cm to a rectangular one of vertical side 36 cm and horizontal side 28 cm (4); shift the mean vertex in the Monte Carlo simulation by $\pm$ 0.4 cm (5). The largest change from (4) is about 5% and from (5) 4%.

- Hadron energy scale and angle. The hadron angle γ_H is calculated using equation (5) and does not depend on the overall hadronic energy scale directly. However it would be affected if there were a local variation which caused the $E - p_Z$ and p_X, p_Y components to be affected differently. To check this effect we have smeared the hadronic energy in each cell in the Monte Carlo simulation by an amount which gives on average an additional 5% smearing in resolution in $E - p_Z$ and p_X, p_Y (6). This change is consistent with our knowledge of the uncertainty in the hadron energy scale from studying DIS jets balancing the electron in transverse momentum and hard photoproduction events with two transverse momentum balanced jets. The largest change in F_2 from this check is just under 10% in some low y bins. The DA DIS acceptance also depends on the value of the y_{JB} cut and to estimate the uncertainty from this source we have varied the value of the cut from the standard value of 0.04 to 0.02 and 0.06 (7). This produces one of the largest sources of uncertainty - with changes between 6 and 20% in some low y bins with a maximum of 28% in the highest x bin at 500 GeV^2. Although the DA method does not depend on the hadronic energy scale directly, it does enter in the cuts. We have checked, by shifting the hadronic energy scale by 5% in the Monte Carlo, that this produces a smaller change everywhere than those already considered under this heading.

- Diffractive events. As we have explained in the previous section diffractive like events are not included in the ARIADNE Monte Carlo sample. To estimate the uncertainty from this omission we unfold with the mixture of ARIADNE and POMPYT (8). The average change is $2 - 3\%$.

- To assess the uncertainty in the unfolding from the particular choice of PDFs we have unfolded with the ARIADNE Monte Carlo using MRSD$'_0$ rather than the standard MRSD$'_-$ (9). The average change is less than 1% but it can rise to about 4% in some high y bins.

- To check the uncertainty in the unfolding method itself we take the difference between two unfolding algorithms (10). The largest changes are around 5%.

- To assess the uncertainty in the estimation of F_L we take the largest change calculated using the following PDF parameterisations: MRSD$'_0$, MRSD$'_-$, GRV(HO), MTB1, MTB2 (11). The change is only visible in the low Q^2 high y bins where it can reach 6%.

The bin-by-bin systematic errors quoted in Tables 1 and 2 are calculated by adding in quadrature all the 11 checks listed above. Figure 11F shows the total relative systematic error as a function of y for Q^2 bins between 8.5 and 250 GeV^2 in which the systematic error is

usually dominant. In this and the other plots in the figure, solid circles indicate bins in which the systematic error is larger than the statistical error and open circles for the opposite case. It can be seen that the errors tend to be largest in the edge bins at high and low values of y. The other plots show the contribution to the total systematic error as follows: (A) electron finding and photoproduction background (1) $\oplus$ (2) $\oplus$ (3); (B) electron angle measurement (4) $\oplus$ (5); (C) hadron angle measurement (6) $\oplus$ (7); (D) final state and unfolding (8) $\oplus$ (9) $\oplus$ (10) and (E) F_L error (11) where the numbers in brackets refer to the individual changes above and $\oplus$ indicates addition in quadrature. From these plots the following conclusions can be drawn: electron finding and background subtraction uncertainties contribute substantially to the systematic error in only a few high y bins; the electron angle measurement is well understood; the F_L and general unfolding uncertainties make a rather small contribution to the systematic error; the biggest uncertainties come from the determination of γ_H at small values of y.

We have also made the following variations in the event selection cuts and checked that the resulting change in F_2 is within the systematic error as calculated above:

- Increase the cut on E'_e from 5 to 10 GeV;
- Apply a primary vertex cut $-40 < Z_{vtx} < 20$ cm;
- Take the largest change when the lower δ cut is varied from 35 to 30 or 40 GeV.

In addition to the bin-by-bin errors there is an overall normalisation uncertainty of 3.5%, of which 3.3% is from the luminosity determination and 1% from the uncertainty in the first level trigger efficiency. The errors of the F_2 data shown in the figures below do not include the normalisation uncertainty.

8.2.3 Electron method systematic errors

For the electron analysis a similar procedure is followed. First the analysis is repeated without the photoproduction background subtraction, then the change from these F_2 values for each of the changes listed below is calculated. The systematic error is the sum of the differences added in quadrature.

- Electron finder. The neural network electron finder was used in place of the standard one. The changes to F_2 average around 3% and reach 11% only in the bin at $Q^2 = 25$ GeV^2 and $x = 0.00042$.
- Electron energy scale. The largest change when the CAL energy scale in the Monte Carlo is adjusted by $\pm$ 1.5% is taken. The change in F_2 averages less than 5% but is 15% in one bin at 65 GeV^2.
- Vertex position. The largest change when the mean Monte Carlo vertex position is shifted by $\pm$1 cm is taken. (A larger shift is used here than in the corresponding check for the DA method because a larger proportion of events do not have a well measured vertex.) The changes are less than 6% in all bins except one at 35 GeV^2 where it is 9%.
- Box cut. Change of the RCAL box cut from the standard square of side 32 cm to one of side 34 cm (this is not the same as the change made in the DA case because of the need to stay within the region where the energy loss corrections have been measured). The changes are generally less than 4%, except in the bin at $Q^2 = 25$ GeV^2 and $x = 0.00042$ where it is 6%.

- Check on electron event selection. The cut on E'_e is increased from 8 to 10 GeV. The changes are very small except in the lowest x and Q^2 bin where it is 6%.

- Sensitivity to radiative corrections and photoproduction background. The largest change when the lower cut on δ is changed to either 32 GeV or 40 GeV is taken. The changes are almost zero except in the lowest x bin at each Q^2, where they decrease rapidly, as Q^2 increases, from 15% at 8.5 GeV^2 to 2% at 65 GeV^2.

The overall systematic error for the electron F_2 averages about 12%, rising to 25% in some bins at high y. In addition to the systematic error analysis just described, an independent electron F_2 measurement was performed in which the energy loss correction was derived from a comparison of the electron energy measured in the CAL and of its momentum measured by tracking. In the bins with Q^2 above 14 GeV^2, where the measurements were made, the F_2 values agree with those from the standard electron analysis within systematic errors.

9 Results

We first compare the results from the two analyses. In both analyses the events are binned in x and Q^2 and after unfolding the F_2 values are determined at the mean x and Q^2 positions for the events in that bin. However as a byproduct of the unfolding, the modification of the input structure function needed to fit the measured F_2 as a function of x and Q^2 is available. It is thus straightforward to give the F_2 value in a bin at more convenient values of x and Q^2 than their means. These are the values quoted in Tables 1 and 2; typically the shift in the value of F_2 is 5% or less.

Figure 12 shows the F_2 values determined by both the DA and electron methods in the bins with $Q^2 < 80$ GeV^2. At a given Q^2 the F_2 values agree very well with each other, generally within statistical errors. At all Q^2 values the slopes of the data, as functions of x, from the two methods also agree well. Though the events are drawn from overlapping samples the reconstruction methods are different and have different systematic effects. In fact, the agreement between the two methods is the most important systematic check on our results. The ability to perform two independent analyses with one apparatus is one of the strengths of the hermetic detectors at HERA.

We choose the DA results for all Q^2 as the final values for the ZEUS 1993 F_2 data. Details are given in Tables 1 and 2 which show for each bin, the x and Q^2 ranges, the number of observed events, the F_2 values and their statistical and systematic errors, the equivalent number of background events and the F_L corrections. Figure 13 shows the final F_2 data for all Q^2 bins except the one at 5000 GeV^2 in which there is only one measured value. The figure shows that the strong rise of F_2 with decreasing x observed in the 1992 HERA data is confirmed. This behaviour is in striking contrast to the almost constant behaviour seen at larger values of x. The steep rise persists from the lowest Q^2 values upto Q^2 of 500 GeV^2. Figure 14 shows the F_2 values versus Q^2 at fixed values of x showing that the data are in accord with the expected logarithmic scale breaking, now measured in a new regime of high Q^2 and low x. Also shown in this figure are the curves from the MRSD$'_-$ (full line) and MRSD$'_0$ (dashed line) PDFs, which represent roughly the extremes of the parameterisations that fit fixed target data. Figure 15 shows the F_2 data as functions of Q^2, at constant x, but plotted on different scales. A non-zero slope, $dF_2/d\ln Q^2$, is a manifestation of scaling violations. The increase in $dF_2/d\ln Q^2$, and therefore of scaling violations, as x decreases is very clear from Figure 15. Using various approximations to the GLAP evolution equations, or a full QCD fit, the behaviour of $dF_2/d\ln Q^2$ can be used

to estimate the gluon momentum density distribution in the proton. A more detailed study of this aspect of our data is in progress [43].

10 Discussion

In this section we first discuss in more detail the comparison of the ZEUS F_2 results with calculations of F_2 based on PDF parameterisations; then comment in a more quantitative way on the rise of F_2 at small x and finally make some observations about the $\gamma^* p$ total cross section derived from the ZEUS F_2 data.

10.1 Comparison of F_2 with PDFs

Returning to Figure 13 which shows F_2 versus x in Q^2 bins, the figure also shows four representative curves from recent PDF evaluations. MRSD'_ (full line) and MRSD'$_0$ (dashed line) [24] have a starting scale for the GLAP evolution of $Q_0^2 = 4$ GeV^2. D'_ has a singular parameterisation for the sea quark and gluon distributions: $xf \sim x^{-n}$ as $x \to 0$ where $n = 0.5$, and D'$_0$ has a constant behaviour: $xf \sim$ const as $x \to 0$ (in both cases at $Q^2 = Q_0^2$). At the lowest values of Q^2 these two PDFs span the ZEUS data, and at Q^2 of 35 GeV^2 and above the data agree with the D'_ curves. The dash-dotted curve shows CTEQ2D' [25] and the dotted curve MRSA [44]. Both these PDFs have singular gluon distributions but with $n \sim 0.3$, for $Q_0^2 = 4$ GeV^2 and are typical of recent PDF evaluations that have included the 1992 HERA data among the data sets used to determine their parameters. Both give good representations of our data at Q^2 values of 25 GeV^2 and upwards. In the lowest Q^2 bins the MRSA curves lie slightly above the ZEUS data, whereas the CTEQ2D' curves follow the data. For all these PDF evaluations of F_2 four quark flavours were used and all were assumed massless.

Figure 16 shows the F_2 data together with the GRV(HO) [26] PDF calculation (full curve), in which the PDFs are evolved from a very low scale of $Q_0^2 = 0.3$ GeV^2, starting with valence-like parton distributions. In this case much of the steep rise in F_2 at low x is generated dynamically by the long GLAP evolution in Q^2 from Q_0^2 to the measured values. In the four lowest Q^2 bins the GRV curves lie above the measured F_2 values, at higher Q^2 values the calculation and data are in agreement. Recently Glück et al. [45] have drawn attention to the importance of the treatment of the heavy quark threshold behaviour in the calculation of F_2 in the HERA Q^2 range. In Figure 16 we show as dashed curves the GRV(HO) calculations of F_2 for the Q^2 values up to 50 GeV^2 and $x < 10^{-2}$, modified to take account of the c quark mass [46]. The effect of the inclusion of heavy quark mass is to lower the GRV(HO) curve by about 10%, which brings the calculation closer to the ZEUS F_2 data.

10.2 Rise of F_2 at low x

In perturbative QCD F_2 was shown to grow faster than any power of $\ln(1/x)$ as $x \to 0$ [47], and the qualitative feature of a rapid rise of structure functions at small x was anticipated by calculations in which only valence-like distributions of partons were evolved from very small Q^2 [48]. Summations of the leading powers of $\ln(1/x)$ had also predicted the gluon distribution to rise as $xg(x, Q^2) \sim x^{-n}$ where n is of the order of 0.5 [49]. To investigate more quantitatively how rapidly F_2 is varying with x at small x values we have made some simple fits to the data

in the Q^2 bins from 8.5 to 500 GeV^2. We have tried fits with a form

$$F_2(x,Q^2) = A(Q^2) + B(Q^2)x^{-n(Q^2)}. \tag{10}$$

Given the small number of data points at each Q^2, the results for the parameters are strongly correlated unless further assumptions are made. For example, fixing A at about 0.3 (for all Q^2) gives rough agreement at large x with the values of F_2 from the NMC experiment [4] (measured up to Q^2 of about 30 GeV^2). For this fit and for fits with fixed n we find acceptable representations of the ZEUS data at Q^2 up to 500 GeV^2 with the power n in the range 0.3 to 0.6.

A compact parameterisation of the ZEUS data at all Q^2 values is provided by the expression:

$$F_2 = (1-x^2)^4[0.35 + 0.017x^{-(0.35+0.16log_{10}Q^2)}]. \tag{11}$$

This functional form has been chosen because it also gives a reasonable representation of the data at larger x values from the NMC experiment. The parameterisation and the ZEUS F_2 data are shown in Figure 17.

10.3 F_2 and $\sigma_{tot}(\gamma^* p)$

Neglecting contributions from Z^0 exchange, the DIS cross section can be thought of in terms of the flux of virtual photons times the total cross section, $\sigma_{tot}(\gamma^* p)$, for scattering of the virtual photon on the proton [50]. $\sigma_{tot}(\gamma^* p)$ is defined in terms of the cross sections for the scattering of transverse and longitudinal photons, σ_T and σ_L respectively, by

$$\sigma_{tot}(\gamma^* p) \equiv \sigma_T(x,Q^2) + \sigma_L(x,Q^2). \tag{12}$$

The photon flux is well defined provided that the lifetime of the virtual photon is large compared to the interaction time, or $x \ll 1/(2m_p R_p)$ where m_p is the mass of the proton and $R_p \simeq 4$ GeV^{-1} its radius [51]. The expression for F_2 in terms of σ_T and σ_L is

$$F_2(x,Q^2) = \frac{Q^2(1-x)}{4\pi^2\alpha}[\sigma_T(x,Q^2) + \sigma_L(x,Q^2)] \tag{13}$$

provided that $4m_p^2x^2 \ll Q^2$. At small x the expression can be rewritten in terms of the total virtual photon proton c.m. energy W (where $W^2 = m_p^2 + Q^2(1/x - 1)$) to give

$$\sigma_{tot}(\gamma^* p) \approx \frac{4\pi^2\alpha}{Q^2} F_2(W,Q^2). \tag{14}$$

The connection between F_2 and $\sigma_{tot}(\gamma^* p)$ has been investigated by others for fixed target DIS data, for example [52].

We use equation 14 to determine $\sigma_{tot}(\gamma^* p)$ from the F_2 data given in Tables 1 and 2. Refering to those tables, we note that the above condition on x is satisfied for all x values at Q^2 values up to 125 GeV^2. Figure 18 shows $\sigma_{tot}(\gamma^* p)$ as a function of W from 50 to 280 GeV for Q^2 values between 8.5 and 125 GeV^2, the errors shown are the statistical and systematic errors added in quadrature. At all these Q^2 values $\sigma_{tot}(\gamma^* p)$ increases with increasing W, as could have been inferred from the x dependence of F_2. Given the size of the errors the increase is compatible with a linear rise but other functions of W give equally good descriptions of the trend. The magnitude of the slope, $d\sigma_{tot}(\gamma^* p)/dW$, at fixed Q^2 is dominated by the factor of

Q^2 in equation (13). This is shown in Figure 19 where $Q^2 \cdot \sigma_{tot}(\gamma^* p)$ is plotted as a function of W for the data with Q^2 between 8.5 and 125 GeV^2. The data cluster along a narrow band. However note that the bulk of the data are within a limited range of W and Q and that the data for $Q^2 > 125$ GeV^2, satisfying the condition above on x, lie below this band (not shown). The rise with W is in marked contrast to that of the total cross section for *real* photon proton scattering at $Q^2 = 0$, $\sigma_{tot}(\gamma p)$, which exhibits only a slow rise between the fixed target regime ($W < 20$ GeV) and the data from HERA near $W = 200$ GeV [8, 15, 53]. That total cross sections for virtual particles might behave differently to those for real particles and in particular rise rapidly with W has been considered by López and Ynduráin [54].

11 Summary

In this paper we have presented the F_2 analysis of the ZEUS 1993 ep DIS data. For $Q^2 < 80$ GeV^2 the data have been analysed using the electron and double angle methods, which are independent and have different systematic uncertainties. The F_2 values from both methods agree with each other as functions of both x and Q^2. The double angle method has also been used at the higher Q^2 values and we choose this method to give the ZEUS 1993 F_2 values. The data confirm, with improved precision, the strong rise in F_2 as x decreases observed in the first F_2 measurements at HERA in 1992. The rise persists from the lowest Q^2 to values of 500 GeV^2. The ZEUS F_2 data are in accord with logarithmic scaling violations in a new regime of low x and high Q^2.

The data have been compared with recent parton distribution evaluations and we find that the data are best described by those with singular gluon and sea-quark distributions at small x, either parameterised as such or generated dynamically. Relating F_2 at fixed Q^2 as a function of x to the W dependence of the virtual photon proton total cross section shows that $\sigma_{tot}(\gamma^* p)$ rises faster with W than the total cross section for real photon proton scattering.

Acknowledgements

The experiment was made possible by the inventiveness and the diligent efforts of the HERA machine group who continued to run HERA most efficiently during 1993.

The design, construction, and installation of the ZEUS detector has been made possible by the ingenuity and dedicated effort of many people from inside DESY and from the home institutes who are not listed as authors. Their contributions are acknowledged with great appreciation.

The strong support and encouragement of the DESY Directorate has been invaluable.

References

[1] H1 Collab., I. Abt et al., Nucl. Phys. B407 (1993) 515.

[2] ZEUS Collab., M. Derrick et al., Phys. Lett. B316 (1993) 412.

[3] BCDMS Collab., A.C. Benvenuti et al., Phys. Lett. B237 (1990) 592.

[4] NMC Collab., P. Amaudruz et al., Phys. Lett. B295 (1992) 159.

[5] E665 Collab., A. Kotwal, Invited talk at the Workshop on 'The Heart of the Matter' Blois France June 1994, to be published in the proceedings.

[6] E. M. Levin, A. D. Martin, Invited talks at the 'Workshop on DIS and Related Topics', Eilat Israel, February 1994, to be published in the proceedings.

[7] The ZEUS Detector, Status Report 1993, DESY 1993.

[8] ZEUS Collab., M. Derrick et al., Phys. Lett. B293 (1992) 465.

[9] C. Alvisi et al., Nucl. Instr. and Meth. A305 (1991) 30.

[10] C.B. Brooks et al., Nucl. Instr. Meth. A283 (1989) 477; B. Foster et al., Nucl. Instr. Meth. A338 (1994) 254.

[11] A. Andresen et al., Nucl. Inst. and Meth. A309 (1991) 101.

[12] A. Bernstein et al., Nucl. Inst. and Meth. A336 (1993) 23.

[13] A. Caldwell et al., Nucl. Inst. and Meth. A321 (1992) 356.

[14] J. Andruszków et al., DESY 92–066 (1992).

[15] ZEUS Collab., M. Derrick et al., DESY-94-032 (1994), to be published in Z. Phys. C.

[16] K. Piotrzkowski, PhD Thesis University of Cracow 1993, DESY F35D-93-06 (1993).

[17] S. Bentvelsen, J. Engelen and P. Kooijman, Proceedings of the Workshop 'Physics at HERA' vol. 1, DESY 1992, 23; S. Bentvelsen, PhD Thesis University of Amsterdam 1994.

[18] F. Jacquet and A. Blondel, Proceedings of the study of an ep facility for Europe, DESY 79/48 (1979) 391, U. Amaldi ed.

[19] GEANT 3.13: R. Brun et al., CERN DD/EE/84-1 (1987).

[20] HERACLES 4.1: A. Kwiatkowski, H. Spiesberger and H.-J. Möhring, Proceedings of the Workshop 'Physics at HERA' vol. 3, DESY 1992, 1294;
A.Kwiatkowski, H.Spiesberger and H.-J.Möhring, Z. Phys. C50 (1991) 165.

[21] B. Andersson et al., Z. Phys. C43 (1989) 625.

[22] ARIADNE 3.1: L. Lönnblad, Comput. Phys. Commun. 71 (1992) 15.

[23] JETSET 6.3: T. Sjöstrand, Comput. Phys. Commun. 39 (1986) 347;
T. Sjöstrand and M. Bengtsson, Comput. Phys. Commun. 43 (1987) 367.

[24] A. D. Martin, R. G. Roberts and W. J. Stirling, Phys. Lett. B306 (1993) 145.

[25] CTEQ Collab., J. Botts et al., Phys. Lett. B304 (1993) 159.

[26] M. Glück, E. Reya and A. Vogt, Phys. Lett. B306 (1993) 391.

[27] LEPTO 6.1, G. Ingelman, Proceedings of the Workshop 'Physics at HERA' vol. 3, DESY 1992, 1366.

[28] ZEUS Collab., M. Derrick et al., Phys. Lett. B315 (1993) 481.

[29] ZEUS Collab., M. Derrick et al., DESY 94-063 (1994), to be published in Phys. Lett. B.

[30] P. Bruni and G. Ingelman, DESY 93-187 (1993); Proceedings of the Europhysics Conference on HEP, Marseille 1993, 595.

[31] N. N. Nikolaev and B. G. Zakharov, Z. Phys. C53 (1992) 331; A. Solano, PhD Thesis University of Torino 1993, unpublished.

[32] PYTHIA 5.6: H.-U. Bengtsson and T. Sjöstrand, Comput. Phys. Commun. 46 (1987) 43;
T. Sjöstrand, Proc. of Workshop on Physics at HERA Vol. 3 (DESY, 1992) 1405.

[33] H. Abramowicz et al., Phys. Lett. 269B (1991) 465.

[34] T. Sjöstrand and M. van Zijl, Phys. Rev. D36 (1987) 2019.

[35] H. Abramowicz and R. Sinkus, 'Electron Identification with Neural Networks at ZEUS', to be published.

[36] ZEUS Collab., M. Derrick et al., Phys .Lett. 303B (1993) 183.

[37] A. Fürtjes, PhD Thesis University of Hamburg 1993, DESY F35D-93-03.

[38] V. N. Gribov and L. N. Lipatov, Sov. Journ. Nucl. Phys. 15 (1975) 438, 675;
G. Altarelli and G. Parisi, Nucl. Phys. B126 (1977) 298.

[39] R. G. Roberts, 'The structure of the proton', Cambridge University Press (1990), Ch. 5 and references therein.

[40] J. Blümlein DESY-94-044 (1994), to be published.

[41] V. Blobel, Proc. of the 1984 CERN School of Computing, Aiguablawa Spain, published by CERN 1985, 88; G. D'Agostini, DESY-94-099 (1994), to be published.

[42] ZEUS Collab., M. Derrick et al., Z.Phys. C59 (1993) 231.

[43] ZEUS Collab., M. Lancaster, Invited talk at the 27th International Conference on High Energy Physics, Glasgow Scotland July 1994, to be published in the proceedings; ZEUS Collab., in preparation.

[44] A. D. Martin, W. J. Stirling and R. G. Roberts, University of Durham preprint DTP/94/34 (and RAL 94-055) June 1994.

[45] M. Glück, E. Reya and M. Stratmann, Dortmund preprint DO-TH 93/20.

[46] We thank E. Reya and M. Stratmann for providing F_2 values from the GRV parton distributions with c quark mass and threshold effects included.

[47] For a non asymptotically free vector theory: V. N. Gribov and L. N. Lipatov, Yad. Fiz. 15 (1972) 781; Sov. J. Nucl. Phys. 15 (1972) 438. For an asymptotically free vector theory: A. De Rujula et al., Phys. Rev. D10 (1974) 1649.

[48] M. Glück, E. Reya and A. Vogt, Z. Phys. C48 (1990) 471; Z. Phys. C53 (1992) 127.

[49] L. N. Lipatov, Sov. J. Nucl. Phys. 23 (1976) 338; Y. Y. Balitsky and L. N. Lipatov, Sov. J. Nucl. Phys. 28 (1978) 822; E. A. Kureav, L. N. Lipatov and V. S. Fadin, Sov. Phys. JETP 45 (1977) 199.

[50] L. N. Hand, Phys. Rev. 129 (1963) 1834; S. D. Drell and J. D. Walecka, Ann. Phys. (N. Y.) 28 (1964) 18; F. J. Gilman, Phys. Rev. 167 (1968) 1365.

[51] B. L. Joffe, V. A. Khoze and L. N. Lipatov, 'Hard Processes', North Holland (1984) p185.

[52] A. Levy and U. Maor, Phys. Lett. 182B (1986) 108; A. Donnachie and P.V. Landshoff, Z. Phys. C61 (1994) 139.

[53] H1 Collab., T Ahmed et al., Phys. Lett. B297 (1992) 205.

[54] C. López and F. J. Ynduráin, Phys. Rev. Lett. 44 (1980) 1118.

Q^2 GeV^2	Q^2 range	x	x range	Events in bin	Back-ground	F_L corr.	Measured $F_2 \pm$ stat $\pm$ sys
8.5	$7-10$	$4.2\cdot10^{-4}$	$3.0-6.0\cdot10^{-4}$	3005	194	1.017	$1.09 \pm 0.03 \pm 0.10$
		$8.5\cdot10^{-4}$	$6.0-12.\cdot10^{-4}$	2267	52	1.004	$0.87 \pm 0.03 \pm 0.08$
12	$10-14$	$4.2\cdot10^{-4}$	$3.0-6.0\cdot10^{-4}$	2249	95	1.033	$1.27 \pm 0.03 \pm 0.10$
		$8.5\cdot10^{-4}$	$6.0-12.\cdot10^{-4}$	2870	55	1.007	$1.02 \pm 0.02 \pm 0.10$
		$1.6\cdot10^{-3}$	$1.2-2.0\cdot10^{-3}$	1799	3	1.002	$0.81 \pm 0.02 \pm 0.11$
		$2.7\cdot10^{-3}$	$2.0-3.6\cdot10^{-3}$	1098	<3	1.001	$0.73 \pm 0.03 \pm 0.17$
15	$14-20$	$4.2\cdot10^{-4}$	$3.0-6.0\cdot10^{-4}$	1177	67	1.069	$1.21 \pm 0.04 \pm 0.18$
		$8.5\cdot10^{-4}$	$6.0-12.\cdot10^{-4}$	2078	57	1.013	$1.12 \pm 0.03 \pm 0.10$
		$1.6\cdot10^{-3}$	$1.2-2.0\cdot10^{-3}$	1516	24	1.003	$0.89 \pm 0.02 \pm 0.08$
		$2.7\cdot10^{-3}$	$2.0-3.6\cdot10^{-3}$	1420	5	1.001	$0.73 \pm 0.02 \pm 0.11$
		$4.7\cdot10^{-3}$	$3.6-6.0\cdot10^{-3}$	407	1	1.000	$0.68 \pm 0.04 \pm 0.09$
25	$20-28$	$4.2\cdot10^{-4}$	$3.0-6.0\cdot10^{-4}$	634	64	1.152	$1.64 \pm 0.10 \pm 0.29$
		$8.5\cdot10^{-4}$	$6.0-12.\cdot10^{-4}$	1384	37	1.026	$1.33 \pm 0.04 \pm 0.11$
		$1.6\cdot10^{-3}$	$1.2-2.0\cdot10^{-3}$	1026	21	1.006	$0.97 \pm 0.03 \pm 0.06$
		$2.7\cdot10^{-3}$	$2.0-3.6\cdot10^{-3}$	1205	<14	1.002	$0.88 \pm 0.03 \pm 0.09$
		$4.7\cdot10^{-3}$	$3.6-6.0\cdot10^{-3}$	622	1	1.001	$0.64 \pm 0.03 \pm 0.10$
35	$28-40$	$8.5\cdot10^{-4}$	$6.0-12.\cdot10^{-4}$	959	62	1.056	$1.56 \pm 0.08 \pm 0.19$
		$1.6\cdot10^{-3}$	$1.2-2.0\cdot10^{-3}$	756	14	1.012	$1.16 \pm 0.06 \pm 0.04$
		$2.7\cdot10^{-3}$	$2.0-3.6\cdot10^{-3}$	947	11	1.004	$0.95 \pm 0.04 \pm 0.06$
		$4.7\cdot10^{-3}$	$3.6-6.0\cdot10^{-3}$	738	1	1.001	$0.83 \pm 0.04 \pm 0.12$
		$7.7\cdot10^{-3}$	$6.0-10.\cdot10^{-3}$	304	<3	1.000	$0.62 \pm 0.04 \pm 0.14$
50	$40-56$	$8.5\cdot10^{-4}$	$6.0-12.\cdot10^{-4}$	568	36	1.124	$1.70 \pm 0.10 \pm 0.32$
		$1.6\cdot10^{-3}$	$1.2-2.0\cdot10^{-3}$	537	17	1.025	$1.33 \pm 0.08 \pm 0.08$
		$2.7\cdot10^{-3}$	$2.0-3.6\cdot10^{-3}$	618	5	1.007	$1.11 \pm 0.06 \pm 0.07$
		$4.7\cdot10^{-3}$	$3.6-6.0\cdot10^{-3}$	570	<14	1.002	$1.02 \pm 0.07 \pm 0.10$
		$7.7\cdot10^{-3}$	$6.0-10\cdot10^{-3}$	402	2	1.001	$0.72 \pm 0.05 \pm 0.12$
		$1.4\cdot10^{-2}$	$1.0-2.0\cdot10^{-2}$	129	<3	1.000	$0.61 \pm 0.07 \pm 0.13$
65	$56-80$	$1.6\cdot10^{-3}$	$1.2-2.0\cdot10^{-3}$	392	39	1.055	$1.29 \pm 0.11 \pm 0.07$
		$2.7\cdot10^{-3}$	$2.0-3.6\cdot10^{-3}$	421	1	1.014	$1.20 \pm 0.09 \pm 0.07$
		$4.7\cdot10^{-3}$	$3.6-6.0\cdot10^{-3}$	374	<14	1.004	$0.92 \pm 0.07 \pm 0.06$
		$7.7\cdot10^{-3}$	$6.0-10\cdot10^{-3}$	361	<3	1.001	$0.75 \pm 0.05 \pm 0.11$
		$1.4\cdot10^{-2}$	$1.0-2.0\cdot10^{-2}$	289	<3	1.000	$0.57 \pm 0.04 \pm 0.12$

Table 1: *ZEUS 1993 F_2 results for the low Q^2 bins. The table contains for each bin: the ranges of x and Q^2; the values of x and Q^2 at which F_2 has been evaluated; the number of measured events prior to corrections; the equivalent number of events from all background sources; the F_L correction and the measured F_2 value and its statistical and systematic errors. Section 7 of the text explains in more detail how the level of background is estimated and in particular subsection 7.3 explains the meaning of the different upper limits given in some bins. The overall normalization uncertainty of 3.5% is not included.*

Q^2 GeV^2	Q^2 range	x	x range	Events in bin	Back-ground	F_L corr.	Measured $F_2 \pm$ stat $\pm$ sys
125	$80-160$	$1.6\cdot10^{-3}$	$1.2-2.0\cdot10^{-3}$	247	24	1.143	$1.57 \pm 0.16 \pm 0.19$
		$2.7\cdot10^{-3}$	$2.0-3.6\cdot10^{-3}$	457	17	1.045	$1.26 \pm 0.08 \pm 0.08$
		$4.7\cdot10^{-3}$	$3.6-6.0\cdot10^{-3}$	426	7	1.011	$1.11 \pm 0.08 \pm 0.05$
		$7.7\cdot10^{-3}$	$6.0-10\cdot10^{-3}$	457	2	1.003	$1.02 \pm 0.08 \pm 0.07$
		$1.4\cdot10^{-2}$	$1.0-2.0\cdot10^{-2}$	515	4	1.001	$0.69 \pm 0.04 \pm 0.07$
		$2.8\cdot10^{-2}$	$2.0-4.0\cdot10^{-2}$	249	< 3	1.000	$0.60 \pm 0.05 \pm 0.10$
250	$160-320$	$4.7\cdot10^{-3}$	$3.6-6.0\cdot10^{-3}$	177	8	1.052	$1.19 \pm 0.13 \pm 0.12$
		$7.7\cdot10^{-3}$	$6.0-10\cdot10^{-3}$	162	2	1.014	$0.81 \pm 0.07 \pm 0.03$
		$1.4\cdot10^{-2}$	$1.0-2.0\cdot10^{-2}$	240	2	1.003	$0.76 \pm 0.06 \pm 0.04$
		$2.8\cdot10^{-2}$	$2.0-4.0\cdot10^{-2}$	242	2	1.001	$0.59 \pm 0.05 \pm 0.05$
		$5.7\cdot10^{-2}$	$4.0-8.0\cdot10^{-2}$	120	< 3	1.000	$0.50 \pm 0.06 \pm 0.12$
500	$320-640$	$7.7\cdot10^{-3}$	$6.0-10\cdot10^{-3}$	62	7	1.062	$0.86 \pm 0.14 \pm 0.18$
		$1.4\cdot10^{-2}$	$1.0-2.0\cdot10^{-2}$	90	0	1.014	$0.71 \pm 0.08 \pm 0.04$
		$2.8\cdot10^{-2}$	$2.0-4.0\cdot10^{-2}$	99	0	1.002	$0.63 \pm 0.08 \pm 0.05$
		$5.7\cdot10^{-2}$	$4.0-8.0\cdot10^{-2}$	99	0	1.000	$0.48 \pm 0.06 \pm 0.07$
		0.11	$8.0-16\cdot10^{-2}$	37	0	1.000	$0.32 \pm 0.05 \pm 0.10$
1000	$640-1280$	$1.4\cdot10^{-2}$	$1.0-2.0\cdot10^{-2}$	39	4	1.055	$0.84 \pm 0.13 \pm 0.20$
		$2.8\cdot10^{-2}$	$2.0-4.0\cdot10^{-2}$	28	0	1.010	$0.48 \pm 0.08 \pm 0.05$
		$5.7\cdot10^{-2}$	$4.0-8.0\cdot10^{-2}$	32	0	1.002	$0.41 \pm 0.07 \pm 0.03$
		0.11	$8.0-16\cdot10^{-2}$	33	0	1.000	$0.36 \pm 0.06 \pm 0.04$
2000	$1280-2560$	$2.8\cdot10^{-2}$	$2.0-4.0\cdot10^{-2}$	18	0	1.040	$1.01 \pm 0.48 \pm 0.47$
		$5.7\cdot10^{-2}$	$4.0-8.0\cdot10^{-2}$	13	0	1.007	$0.39 \pm 0.10 \pm 0.08$
		0.11	$8.0-16\cdot10^{-2}$	16	0	1.001	$0.36 \pm 0.10 \pm 0.02$
5000	$2560-10000$	0.11	$8.0-16\cdot10^{-2}$	10	0	1.007	$0.46 \pm 0.21 \pm 0.11$

Table 2: *ZEUS 1993 F_2 results for the high Q^2 bins. See the caption to Table 1 for details of the entries. The Z^0 corrections for the F_2 values in the highest Q^2 bins are as follows: $Q^2 = 1000$ GeV^2, 0.980, 0.983, 0.987, 0.991; $Q^2 = 2000$ GeV^2, 0.940, 0.950, 0.966; $Q^2 = 5000$ GeV^2, 0.82. For each Q^2 bin the corrections are given in order of increasing x.*

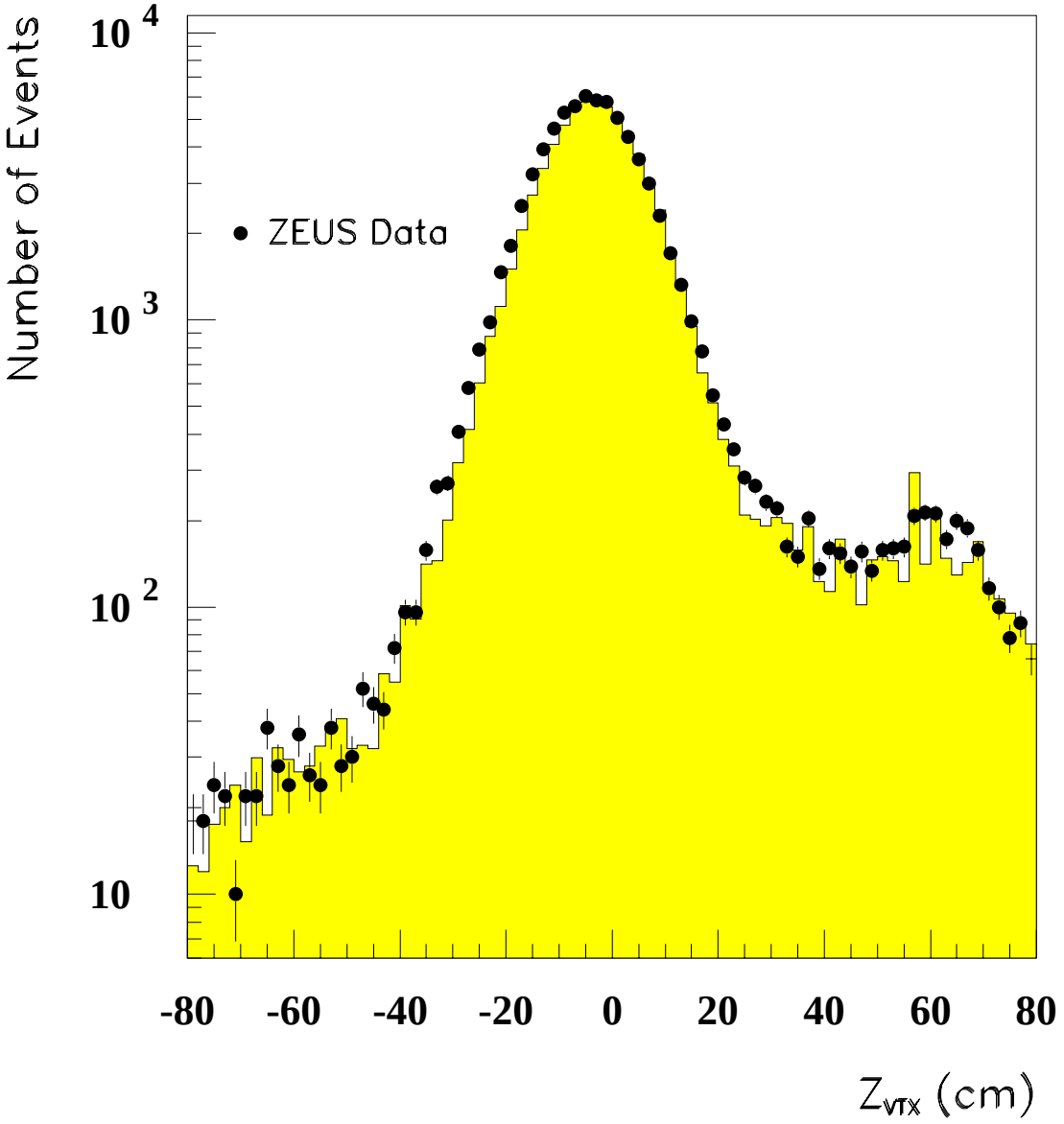

Figure 1: *The Z_{vtx} distribution for the DA DIS data sample (solid circles) and from the ARIADNE Monte Carlo sample (histogram), generated according to non-diffractive photoproduction events.*

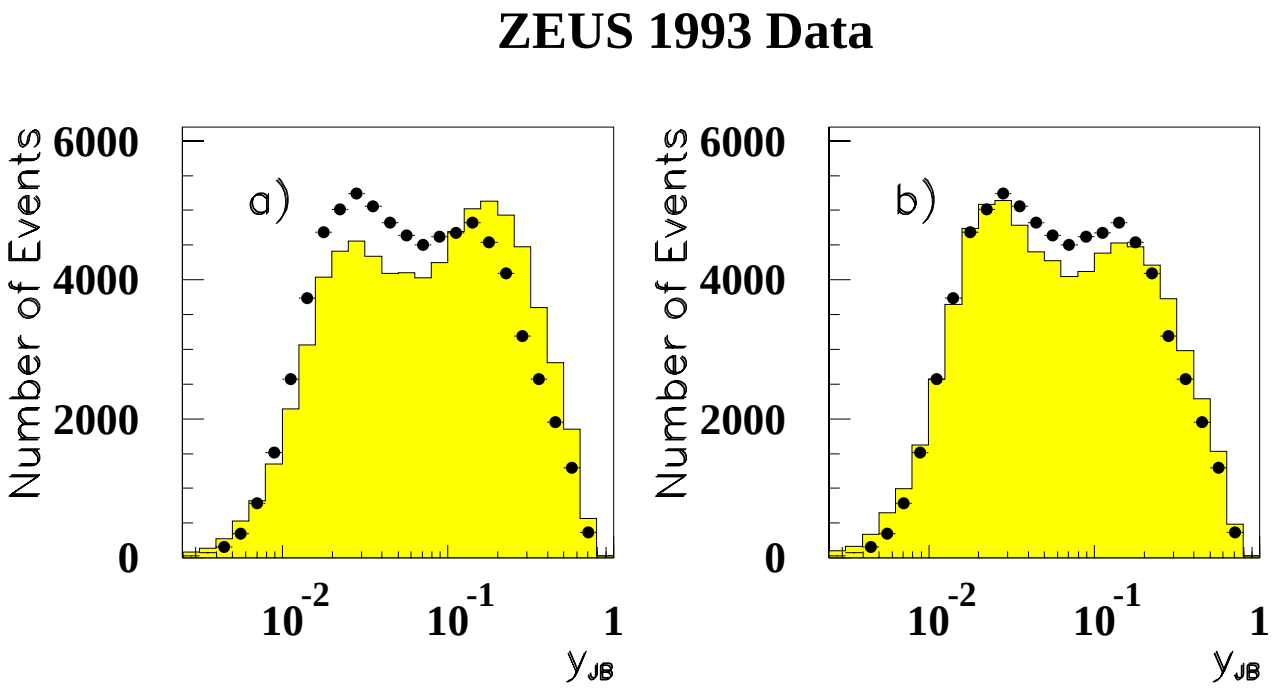

Figure 2: *Distributions of y_{JB} for the DA method before the cut on y_{JB} is applied; (a) shows the data (solid circles) compared to the ARIADNE simulation with the MRSD'_ PDF (histogram); (b) the data compared to the same simulation but now reweighted to the measured F_2. In both cases the number of simulated events has been normalised to the data.*

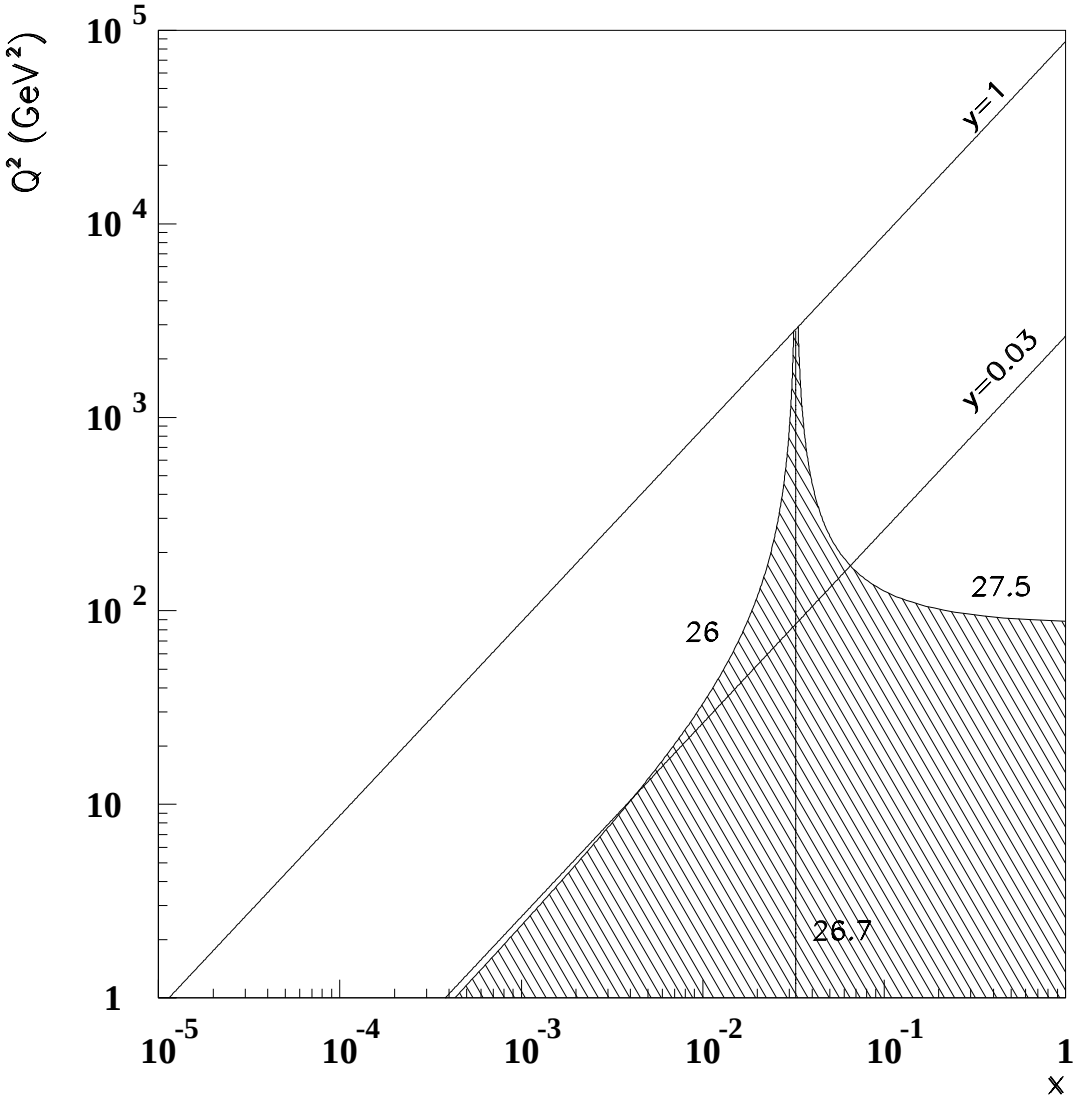

Figure 3: $x - Q^2$ *plane showing the region of the kinematic peak as the shaded area bounded by the contours corresponding to* E'_e *of 26.0 and 27.5 GeV. The vertical line is the contour for* $E'_e = E_e$*. Lines of constant* y *at 1 and 0.03 are also shown.*

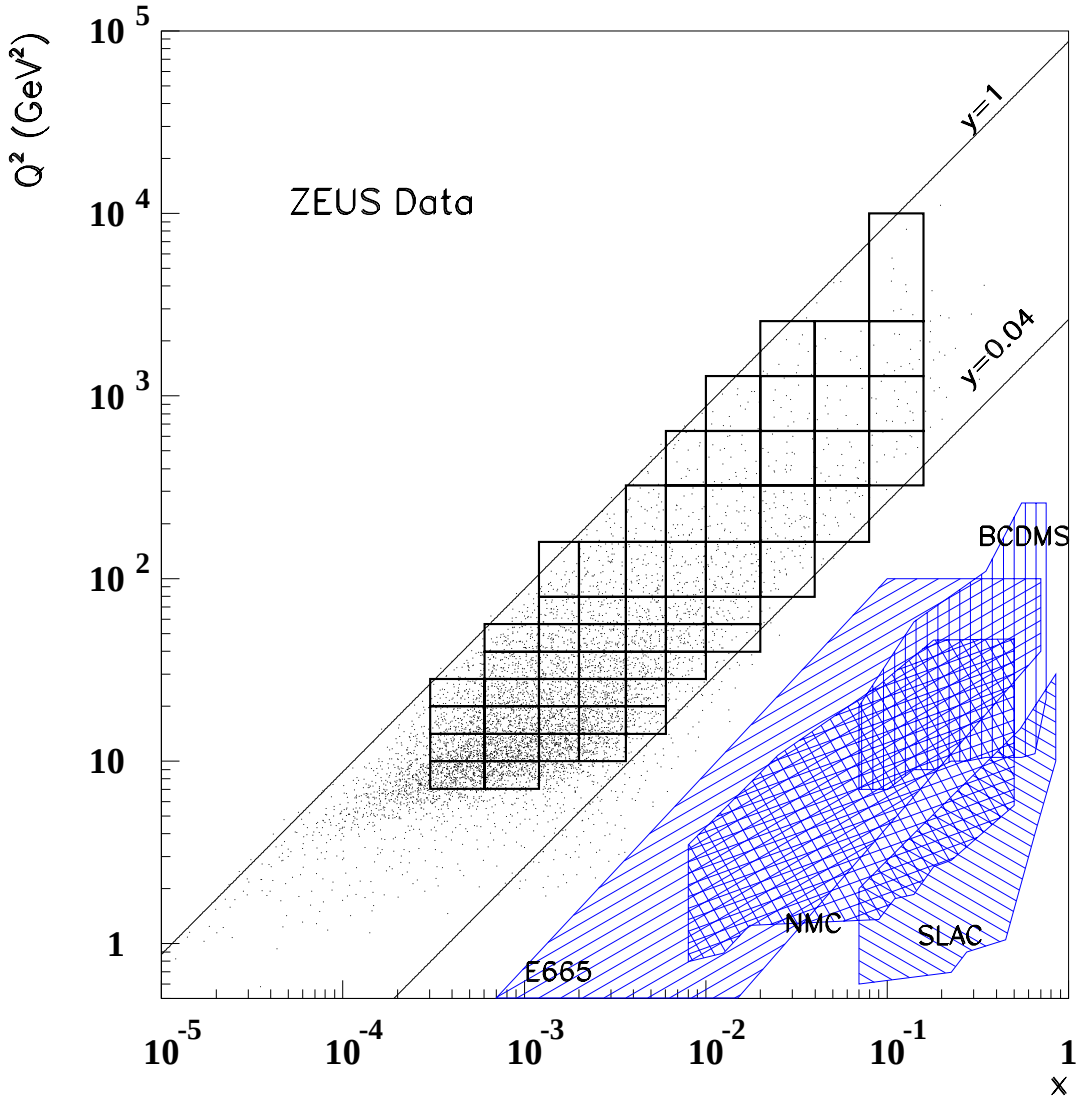

Figure 4: *Distribution of the DA DIS event sample in the $x - Q^2$ plane. Also shown are lines of constant y at 1 and 0.04, the bins in which F_2 is measured and the regions where data from fixed target experiments exist.*

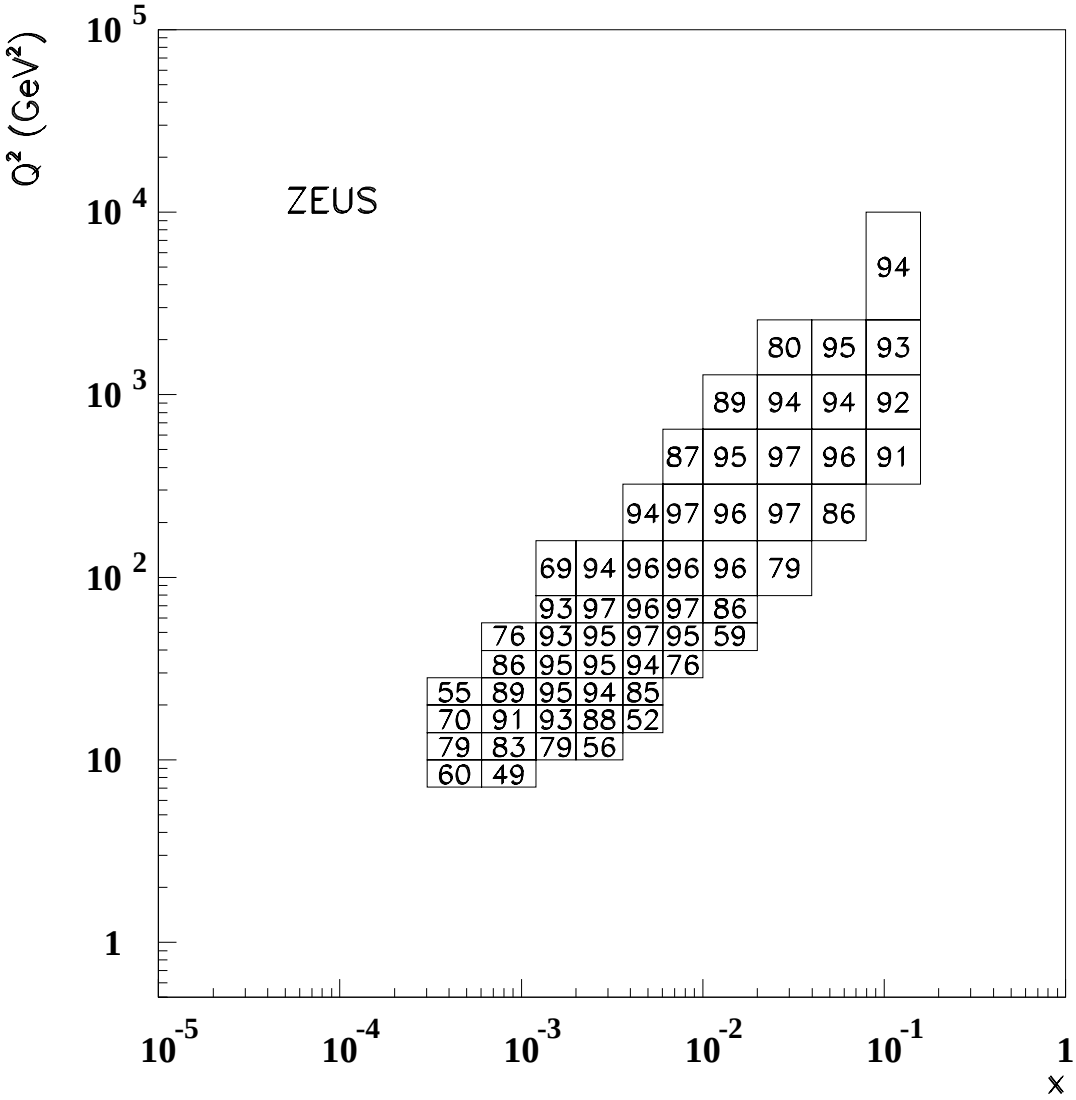

Figure 5: *Overall DIS event selection acceptance (percent) in the selected $x - Q^2$ bins.*

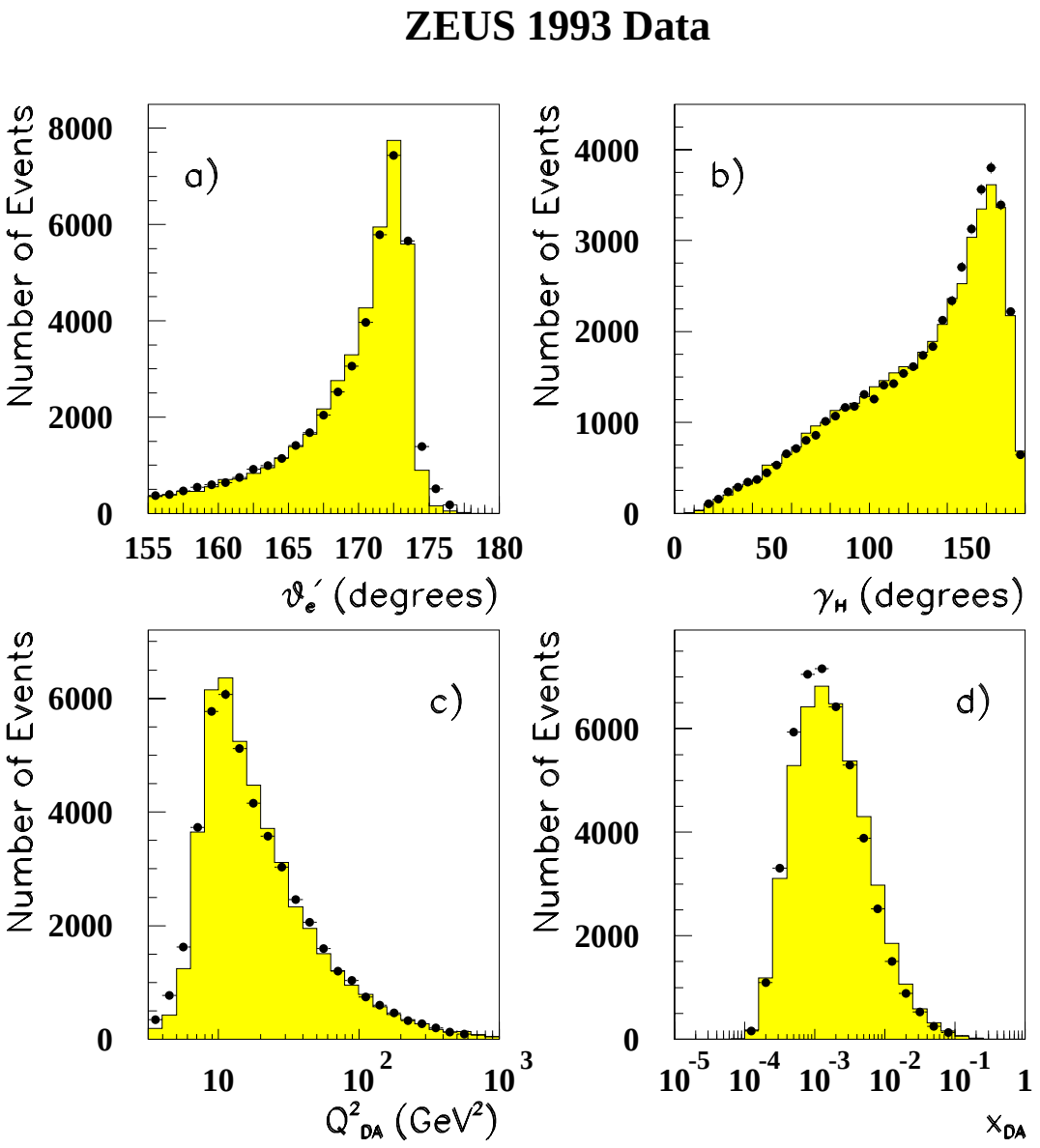

Figure 6: *Distributions of the primary measured quantities and the kinematic variables for the DA DIS sample in the selected bins: (a) θ'_e; (b) γ_H; (c) Q^2_{DA}; (d) x_{DA}. The data (solid circles) are compared to the ARIADNE simulation (histogram), adjusted to our measured F_2 values. The number of simulated events is normalised to the data.*

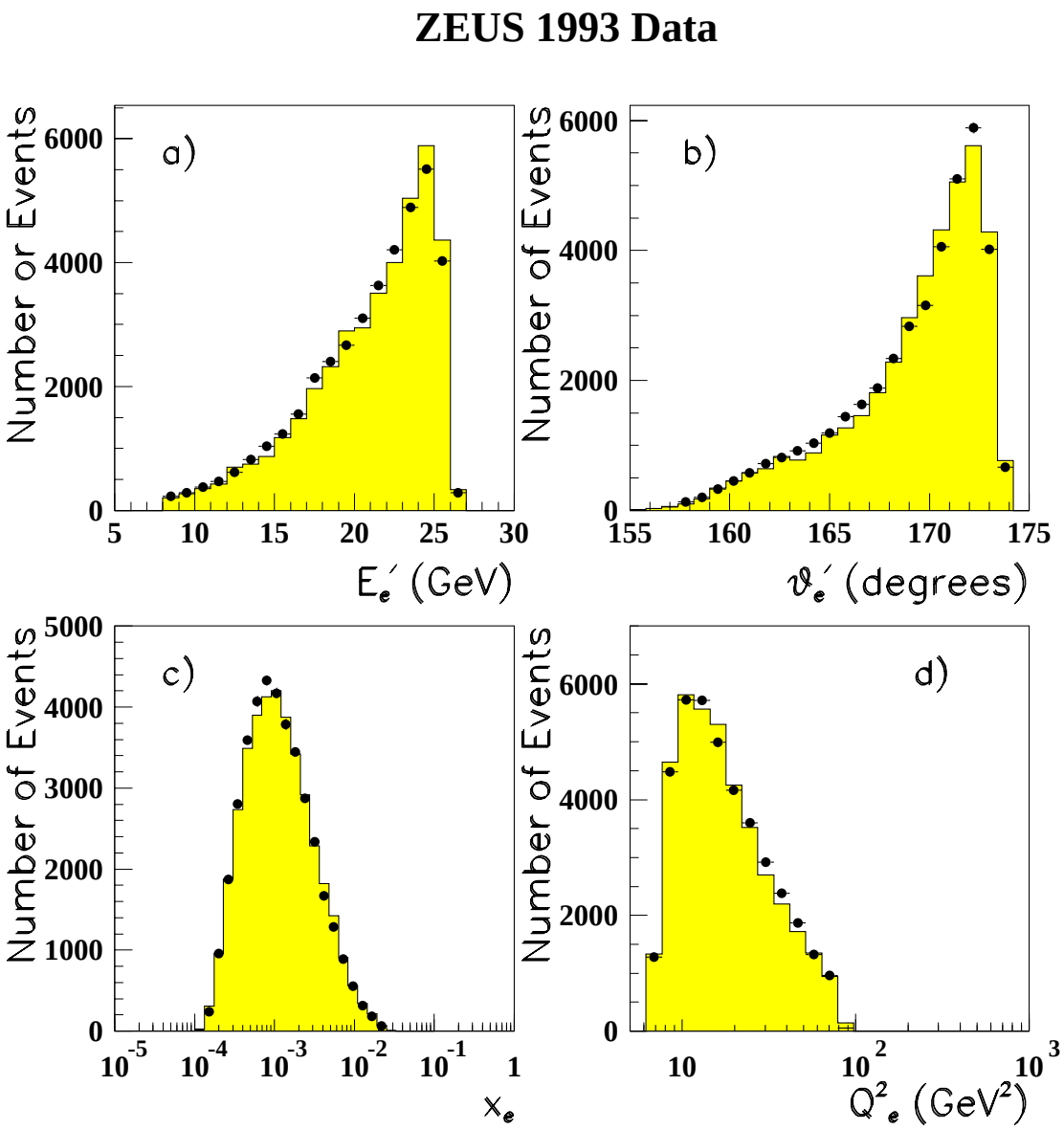

Figure 7: *Distributions of the primary measured quantities and the kinematic variables for the electron DIS sample in the selected bins: (a) E_e' corrected; (b) θ_e'; (c) x_e; (d) Q_e^2. The data (solid circles) are compared to the ARIADNE Monte Carlo event sample adjusted to fit the measured F_2 and normalised to the data (histogram).*

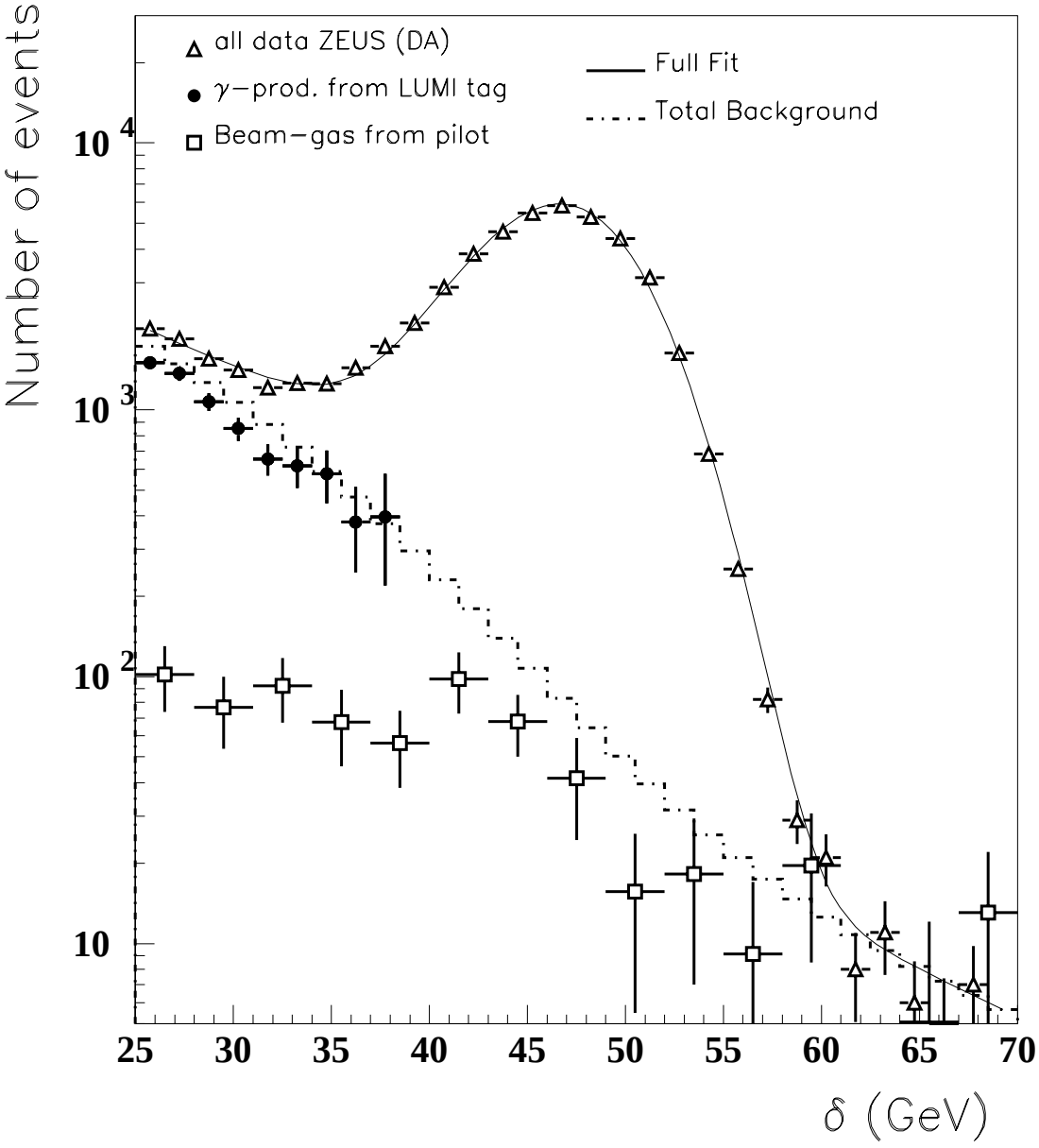

Figure 8: *The distribution of δ for the DA DIS sample before the cut at 35 GeV is applied (triangles), together with tagged photoproduction (solid circles) and beam-gas background (open squares) events satisfying the DIS event selection cuts. The full curve is a fit to all the data and the dash-dotted histogram the function used in the fit to describe the combined background – see section 7.2 for more details.*

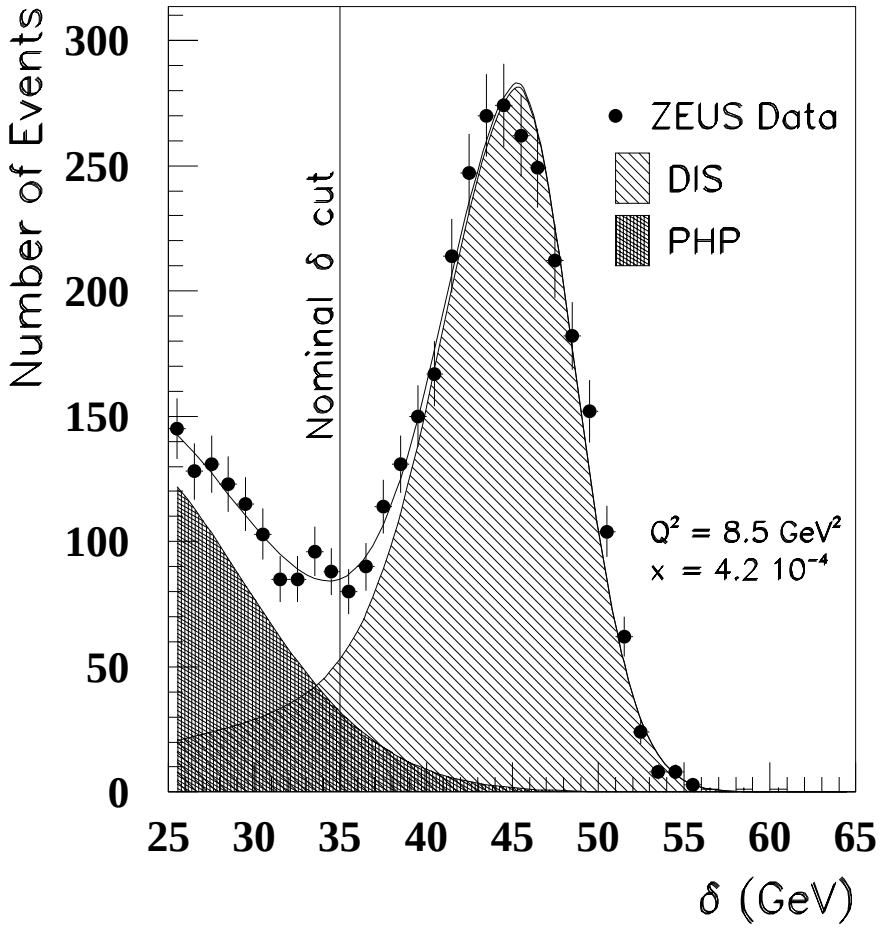

Figure 9: *Example of a fit to the δ distribution in one $x - Q^2$ bin showing how the photoproduction background is estimated. In the figure DIS refers to the DIS signal and PHP to the photoproduction background.*

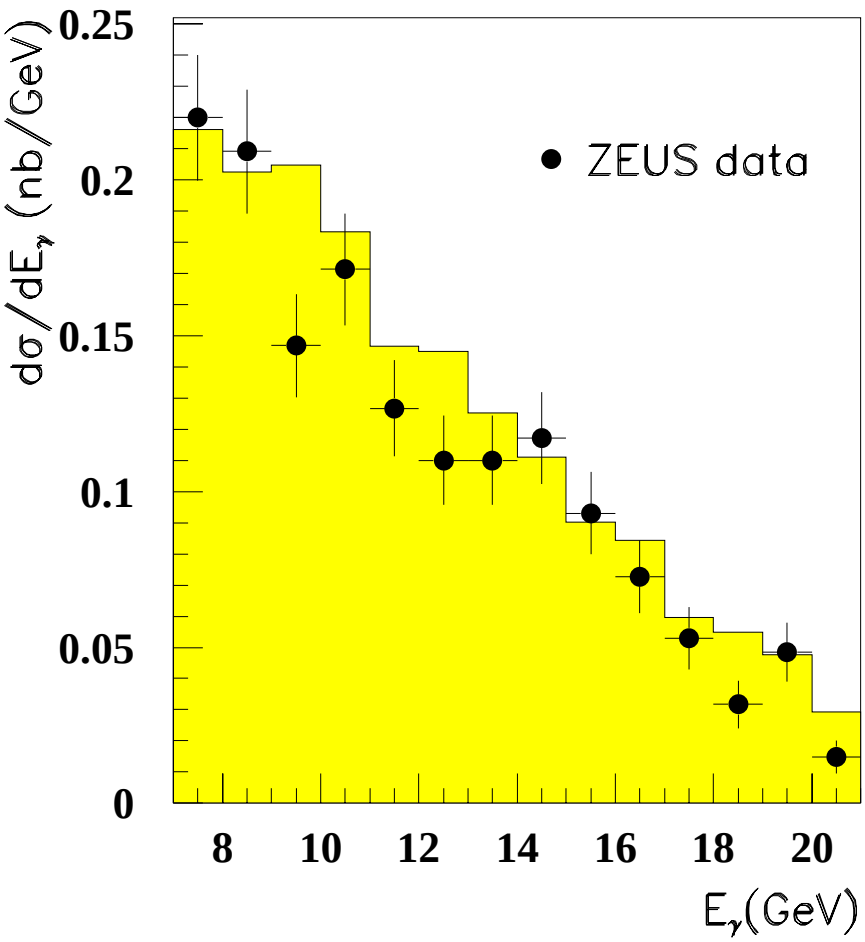

Figure 10: *The differential cross section of E_γ for DIS events in which a hard initial state radiative photon is measured in the luminosity gamma detector. The data is shown as (solid circles) and is compared to an absolute prediction of the HERACLES Monte Carlo simulation (histogram) with $Q_h^2 > 4$ GeV^2.*

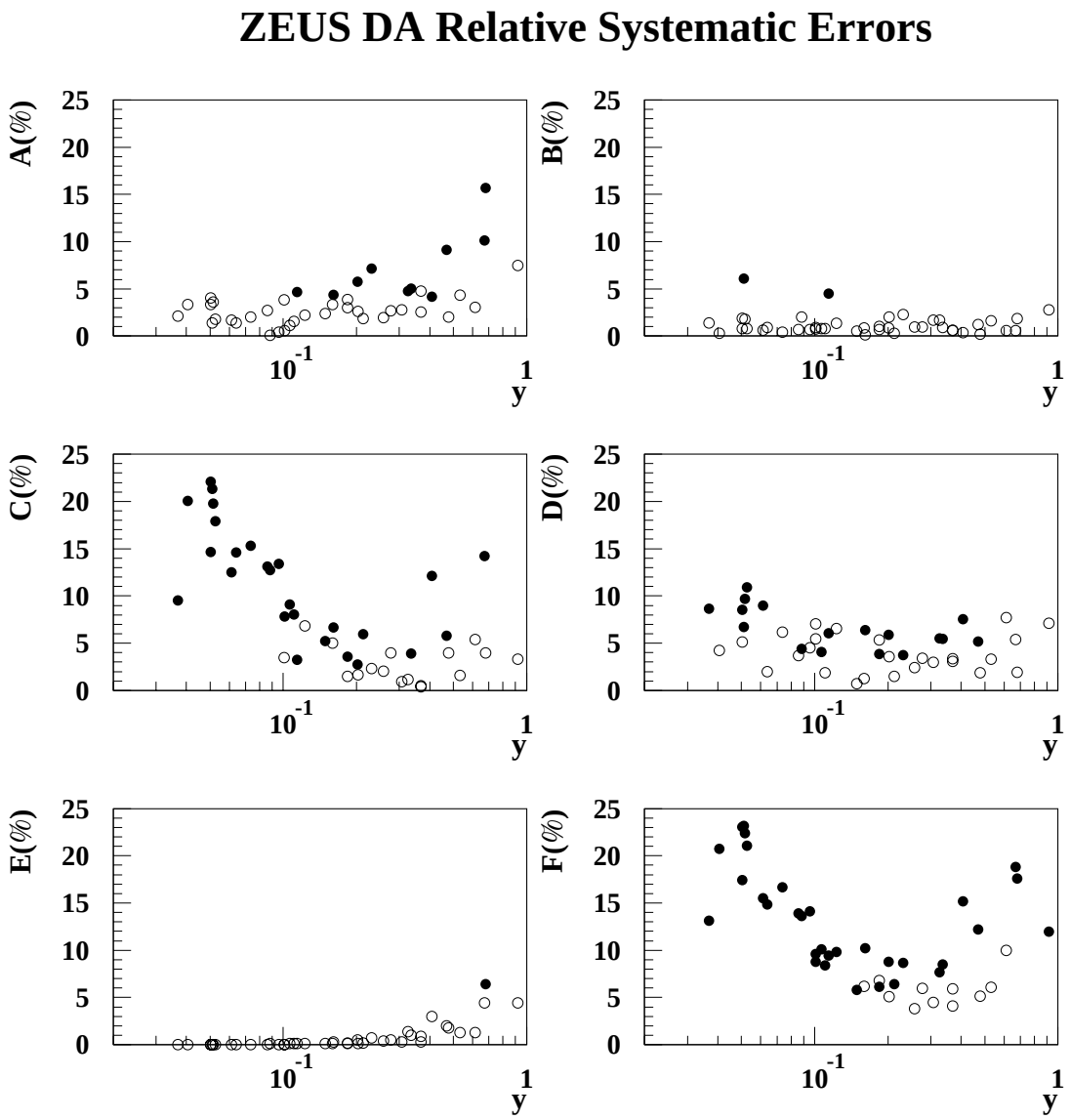

Figure 11: *Relative systematic errors in percent plotted as functions of y for the DA F_2 values in the Q^2 bins between 8.5 and 250 GeV^2. (A) Electron finding and background subtraction errors. (B) Electron angle errors. (C) Errors associated with γ_H and the y_{JB} cut. (D) Final state description and unfolding errors. (E) F_L correction errors. (F) The total systematic error. Open circles indicate that the systematic error (or component) is smaller than the statistical error and solid circles the opposite case. Full details of the error determination are given in section 8.2.2.*

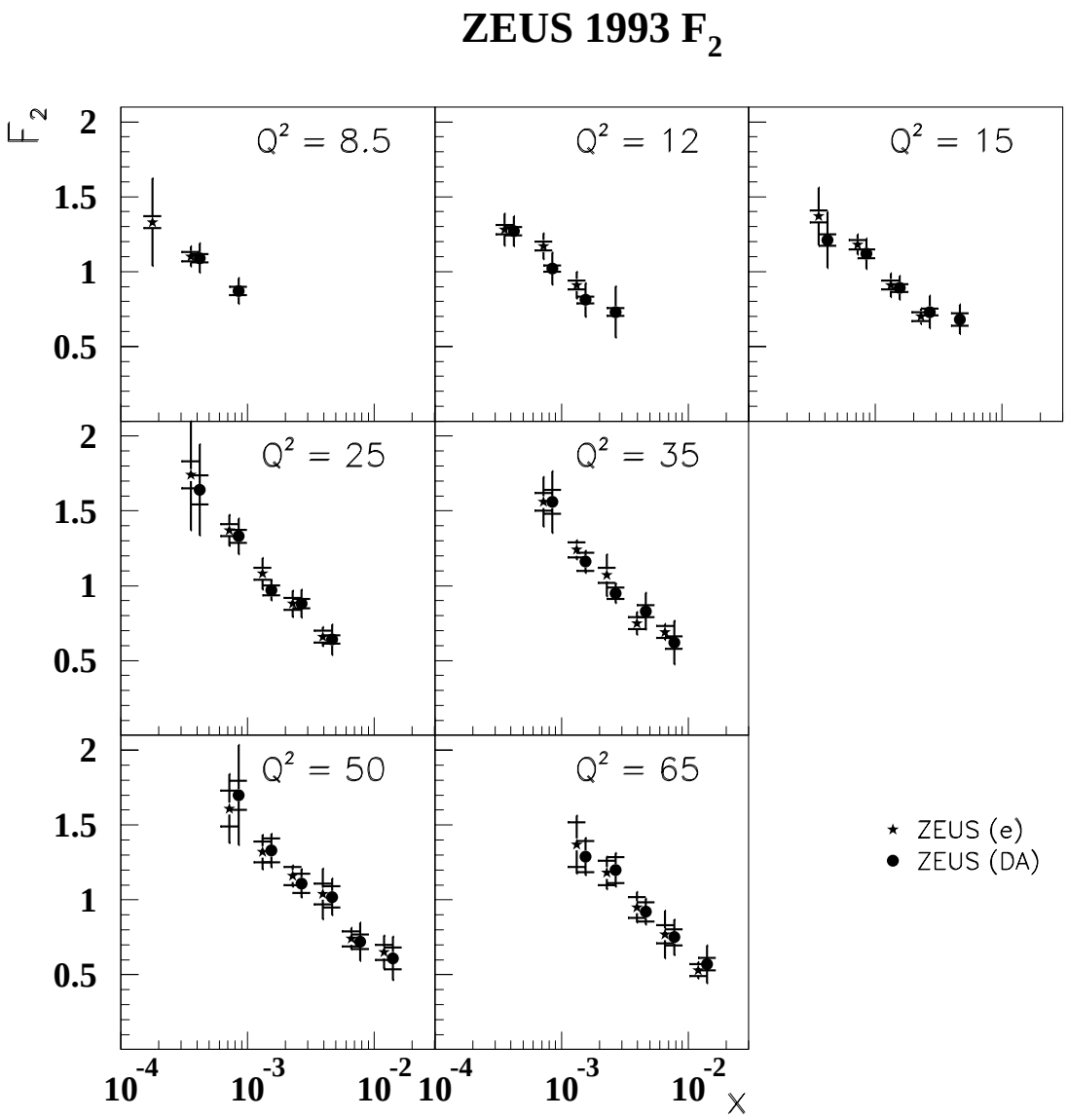

Figure 12: *F_2 values from the DA (solid circles) and electron (stars) methods plotted as functions of x for Q^2 values between 8.5 and 65 GeV^2. The inner error bar shows the statistical error and the full bar the statistical and systematic errors added in quadrature. The overall normalisation uncertainty of 3.5% is not included. Note that for clarity of presentation the electron points have been plotted at x values shifted by 15% to lower values (leftwards).*

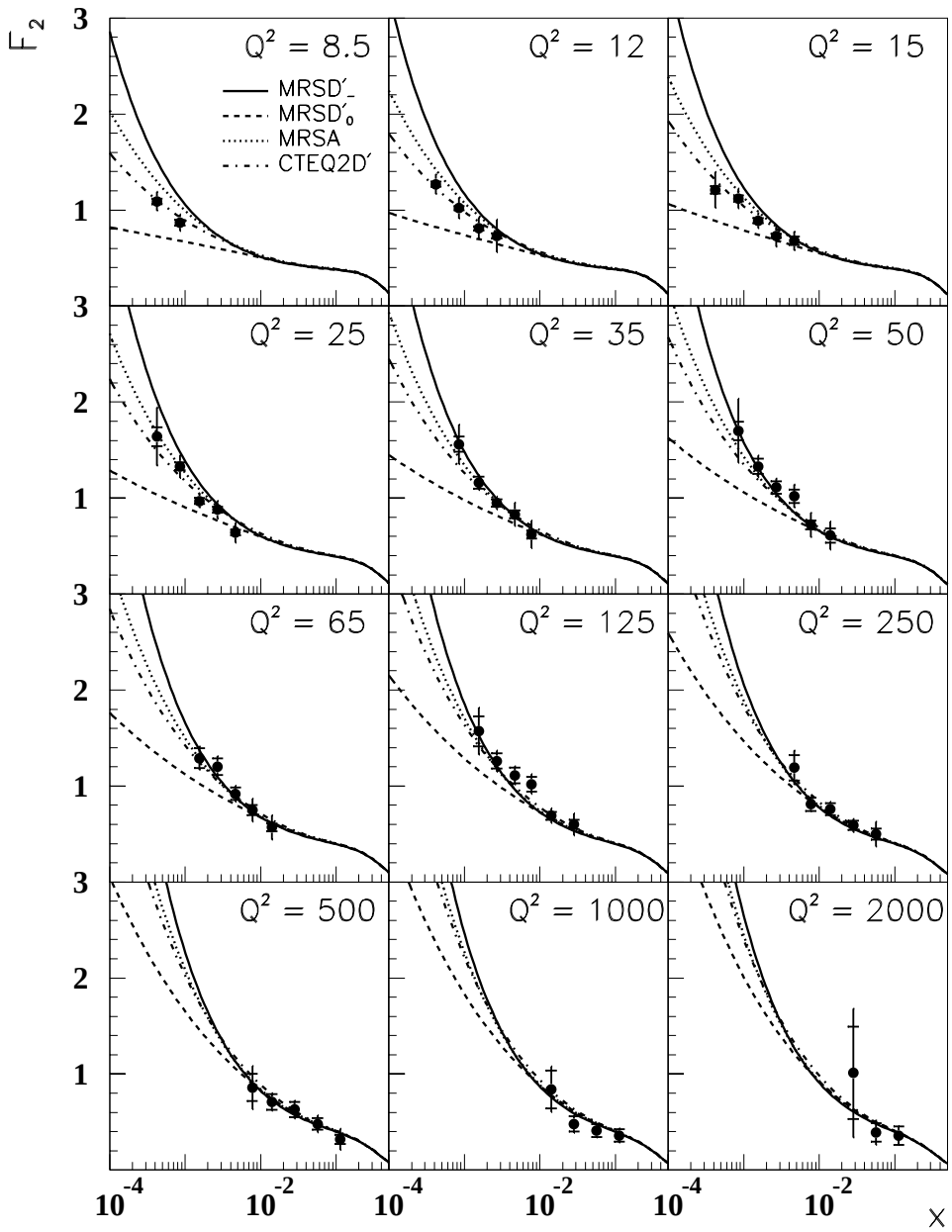

Figure 13: *ZEUS 1993 final F_2 values (solid circles) plotted as functions of x at fixed Q^2 and compared to the following recent PDF calculations: MRSD′_ (full curve), MRSD′$_0$ (dashed curve), CTEQ2D′ (dash-dotted curve) and MRSA (dotted). The inner error bar shows the statistical error and the full bar the statistical and systematic errors added in quadrature. Q^2 is measured in GeV^2. The overall normalisation uncertainty of 3.5% is not included.*

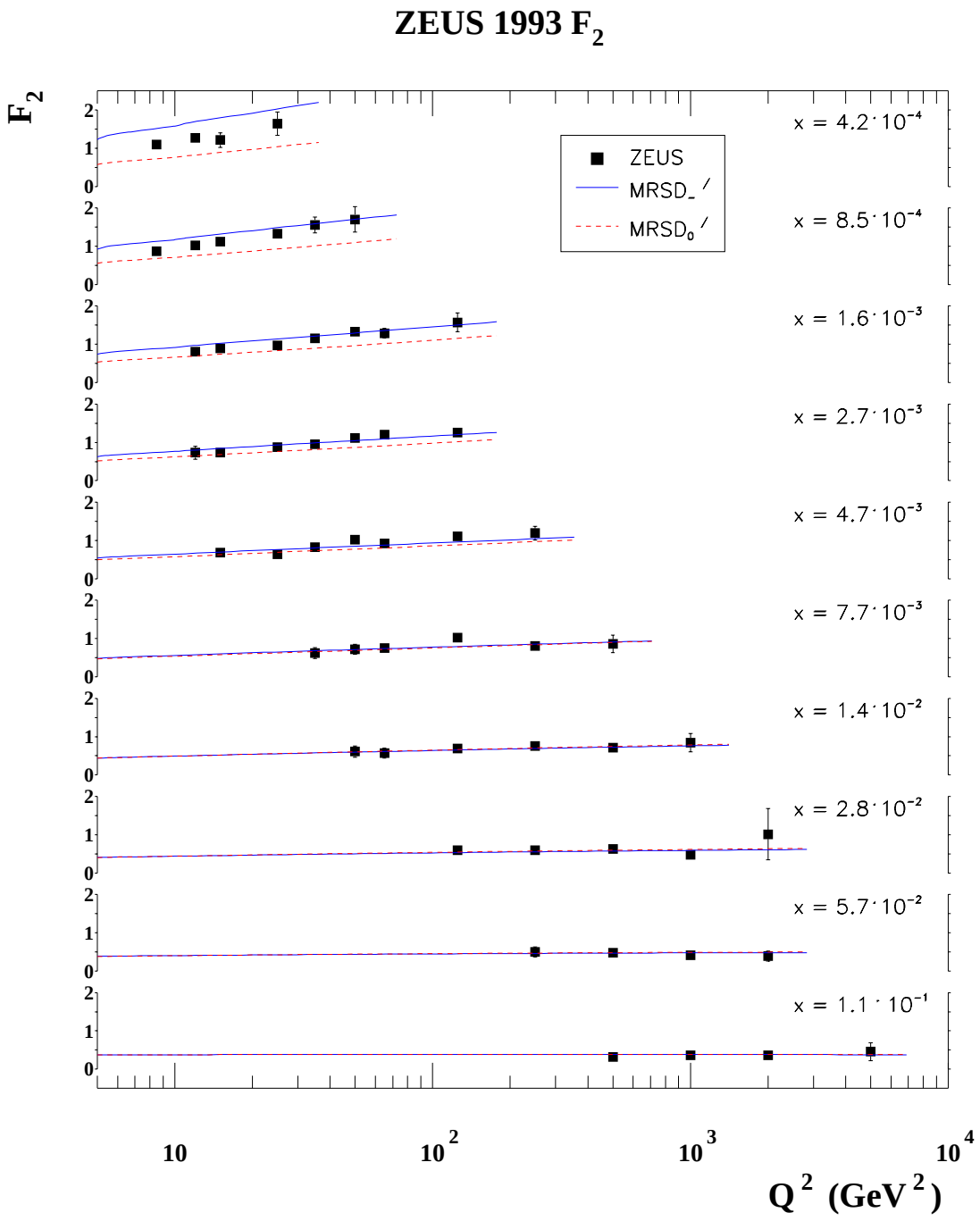

Figure 14: *ZEUS 1993 F_2 data plotted as functions of Q^2 at fixed x, together with MRSD'_ (full curve) and MRSD$'_0$ (dashed curve) calculations - note the broken vertical scale.*

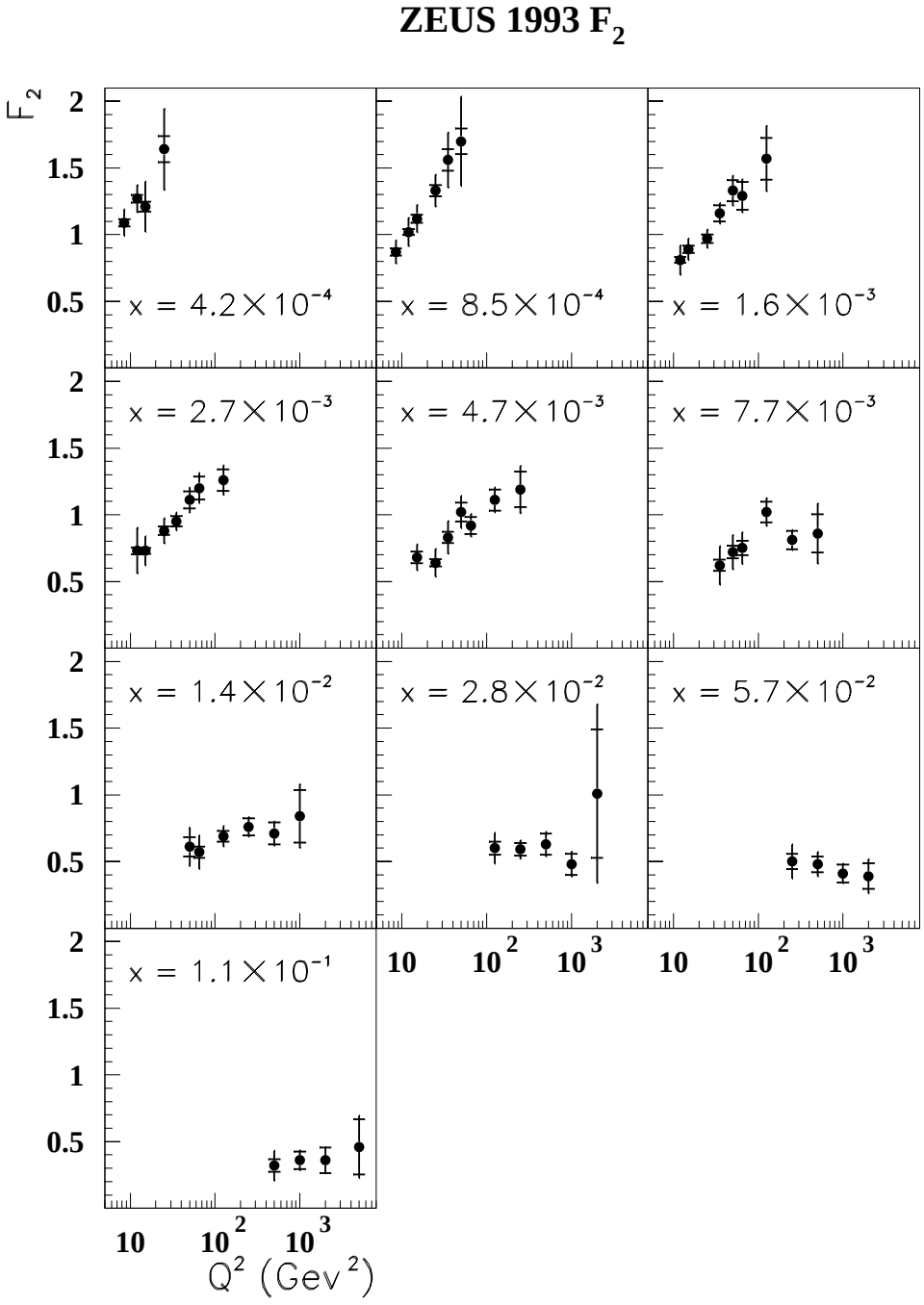

Figure 15: *ZEUS 1993 values for F_2 plotted as functions of Q^2 at fixed x, showing the slopes of F_2 as functions of Q^2 more clearly. The inner error bar shows the statistical error and the full bar the statistical and systematic errors added in quadrature. The overall normalisation uncertainty of 3.5% is not included.*

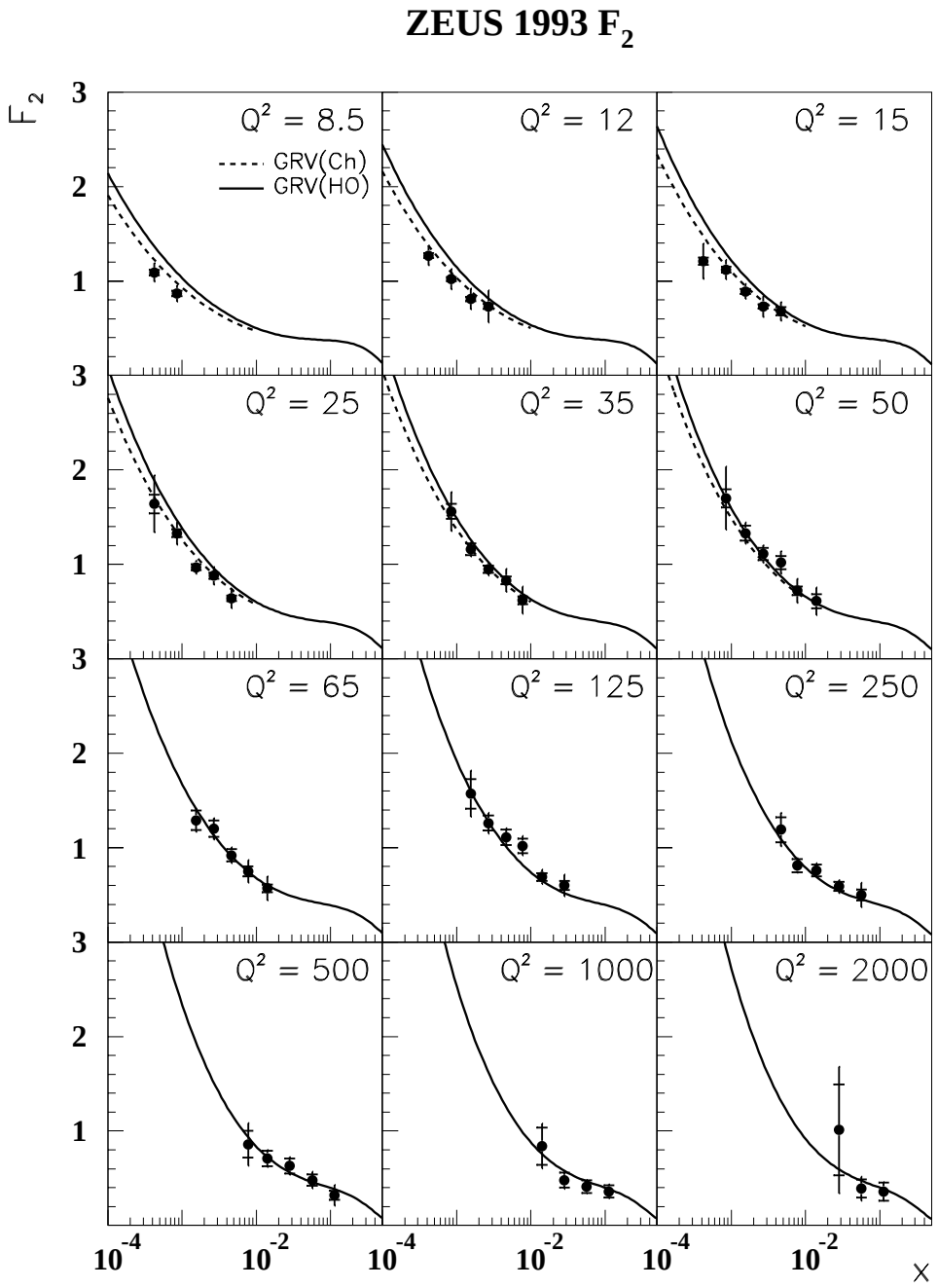

Figure 16: *The ZEUS 1993 F_2 data at fixed Q^2. The full curve shows the GRV(HO) PDF calculation. For the first six Q^2 values the dashed curve shows the GRV(HO) calculation for $x < 10^{-2}$ modified to take account of the finite mass of the c quark. Q^2 is measured in GeV^2.*

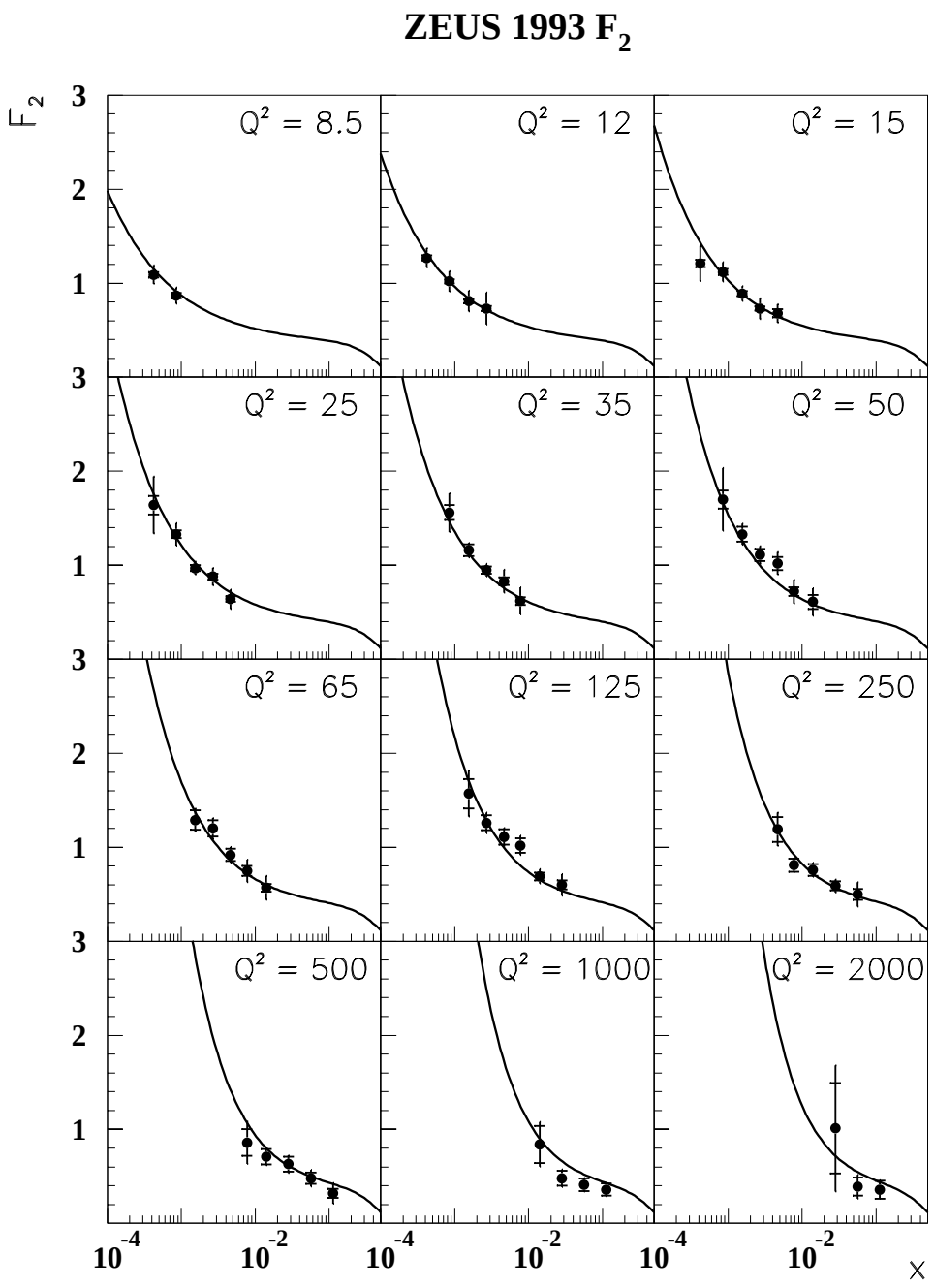

Figure 17: *The ZEUS 1993 F_2 data compared to the compact parameterisation of equation (11) of the text. Q^2 is measured in GeV^2.*

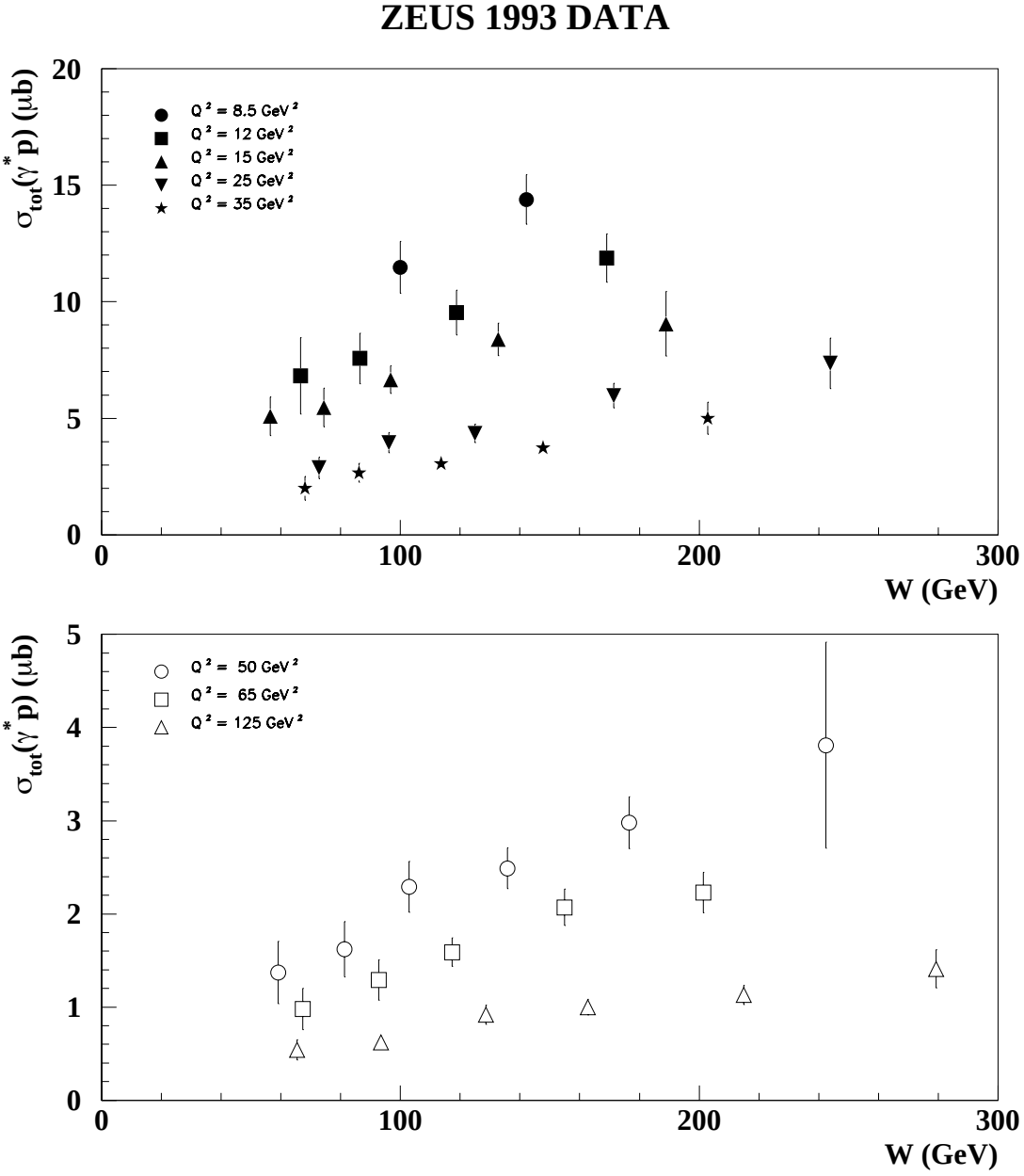

Figure 18: *The virtual photon proton total cross section $\sigma(\gamma^* p)$ as a function of W for the Q^2 values between 8.5 and 125 GeV^2, calculated as described in section 10.3 of the text.*

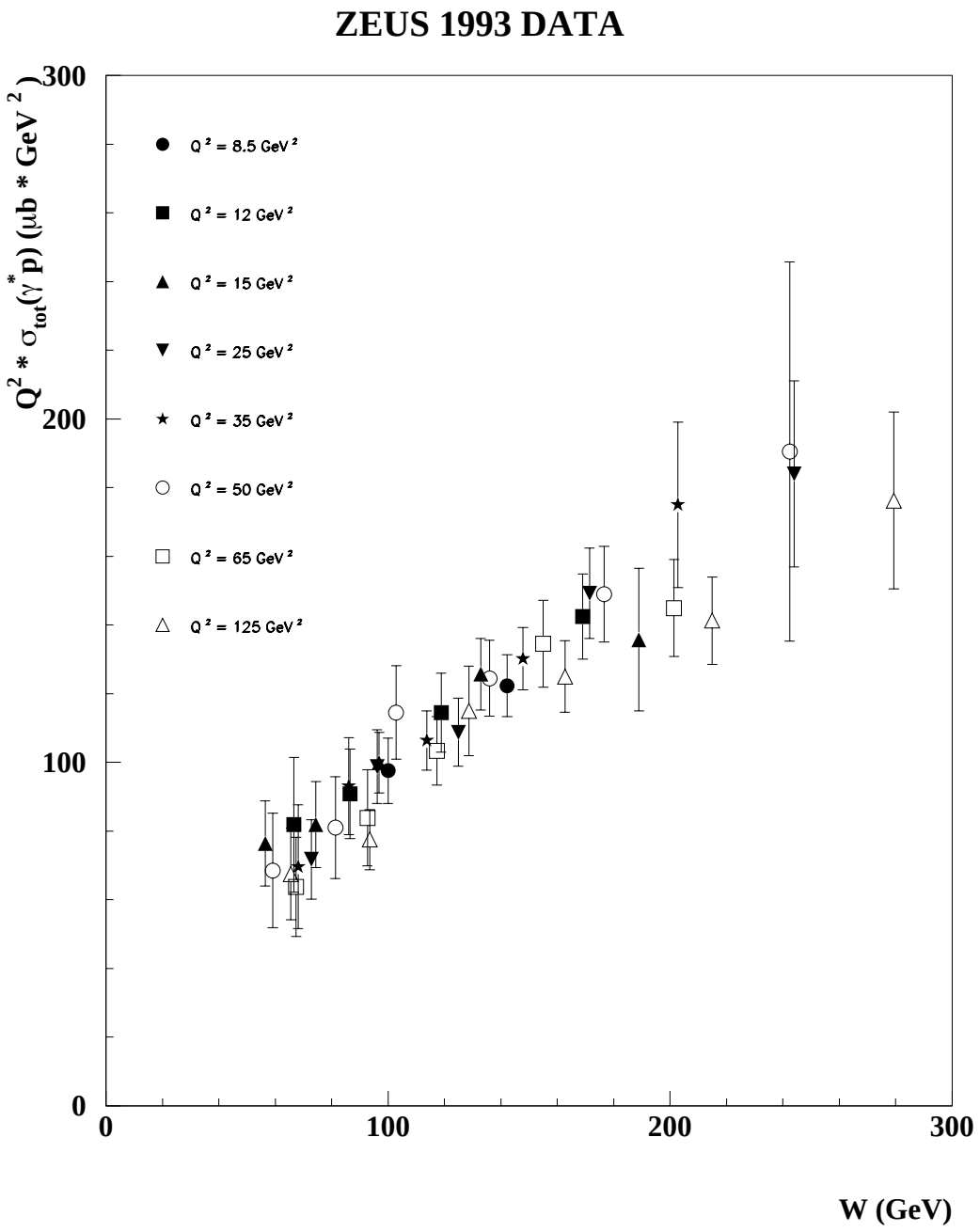

Figure 19: *$Q^2 \cdot \sigma(\gamma^* p)$ as a function of W for the Q^2 values between 8.5 and 65 GeV^2, calculated as described in section 10.3 of the text.*